University of Southern Queensland
Faculty of Health, Engineering and Sciences

Embedded FBG Sensors for Structural Health Monitoring of Advanced Composite Structures

A Thesis submitted by

Joshua Peauril
B.Eng, B.Design

In fulfilment of the requirements of
Master of Engineering Research

2014

ABSTRACT

Fibre reinforced polymer composite materials (FRP) have been used in critical civil infrastructure for several decades due to their attractive strength to weight ratio and ease of manufacturing to meet required design objectives. However, the long-term behaviour of FRP structures is not well understood and the fear of catastrophic failure inhibits the wide-spread use of them. Frequent monitoring, therefore, is essential in order to know the structural integrity and damage status of the structure to give early warning signs. Recent developments in sensor technologies have significantly contributed to the improved health monitoring systems for critical infrastructure. Among those new generation sensors, Fibre Bragg Grating (FBG) sensors have demonstrated their superior properties in Structural Health Monitoring (SHM) of composite structures. This thesis details a conceptual design and application of an embedded FBG sensor network in a representative FRP bridge deck structure and a representative hybrid FRP bridge beam. Sensor embedding methods were developed that save production time and improved the durability of the sensors. The smart deck was tested under Uniformly Distributed Loads (UDL) with increasing simulated damage to show the FBG sensor ability to detect damage. The smart bridge beam was tested under cyclical four point bending and successfully showed FBG sensor ability to detect early signs of fatigue.

Keywords: fibre Bragg grating, structural health monitoring, fibre composite, infrastructure, damage, fatigue

List of Publications during this study

Peauril, J, Epaarachchi, J, Wang, H, Lau, K.T., 2013, *Embedded Fibre Optic Sensors under Multi-axial Loading*, International Conference on Smart Materials and Nanotechnology, Gold Coast.

Ku, H, Peauril, J, Cardona, F, Trada, M, 2014, *Recycling Glass Fibre Composites – Process and Viability*, Journal of Polymer Science. (on review)

Peauril, J, Watt, N, 2014, *Lightweight Fibre Composite Bridges: Pedestrian and Road Applications*, 6th Australian Small Bridges Conference, Sydney.

Peauril, J, Watt, N, 2014, *Lightweight Composite Bridges and Decking Applications*, Research to Reality: Promoting fibre composites in civil infrastructure, USQ, Toowoomba.

Peauril, J, Epaarachchi, J, Wang, H, 2014, Smart FRP Bridge Deck Concept with Embedded Fibre Optic Sensors for Structural Health Monitoring, Composite Structures (submitted)

Certification of Dissertation

I certify that the ideas, designs and experimental work, results, analyses and conclusions set out in this dissertation are entirely my own effort, except where otherwise indicated and acknowledged. The work is original and has not been previously submitted for assessment in any other course or institution, except where specifically stated.

Signed: _____ Date: _____

Joshua Peauril
Student ID: 0039511427

Endorsement by Supervisors

Signed: _____ Date: _____

Dr. Jayantha Epaarachchi
Principle Supervisor

Signed: _____ Date: _____

Prof. Hao Wang
Associate Supervisor

Acknowledgments

I would like to thank those who have helped with the research both officially and unofficially: Dr Jayantha Epaarachchi, Prof Hao Wang and Dr Francisco Cardona for academic advice, Wayne Crowell and Mohan Trada for assistance with testing and technical issues and all of the composites centre (CEEFC) staff and students for their assistance on a daily basis. Special thanks goes to my wife and family, for without their love and support this achievement would not be possible.

Joshua Peauril

Notation

Abbreviation	Meaning
Roman Letters	
CFRP	Carbon fibre reinforced polymer
COV	Coefficient of Variance
E	Elastic modulus or Young's Modulus
FBG	Fibre Bragg grating
FRP	Fibre reinforced polymer
GFRP	Glass fibre reinforced polymer
L	length
M	moment
MSE	Mean Squared Error
R	Radius of curvature
SHM	Structural health monitoring
S.G.	Specific gravity
UDL	Uniformly distributed load
V	Shear force
VARTM	Vacuum assisted resin transfer moulding
VE	Vinyl Ester polymer
VIP or RIP	Vacuum infusion process/resin infusion process
Greek Letters	
δ	Deflection or deformation
ε	strain
Λ	Aperture length
λ	Wavelength
μ	Micro ($x10^{-6}$)
σ	Tensile stress
τ	Shear stress
θ	Angle theta
Other	
$\approx$	Approximately equal to

Contents

1. INTRODUCTION

1.1. Background

Structural health monitoring of fibre composites is a growing area due to the lack of warning signs fibre composites exhibit before brittle failure. Smart materials with embedded sensors can give real-time feedback of the performance of the component and early warning signs of damage or fatigue. Fibre composite solutions, specifically fibre reinforced polymers (FRP), are increasingly adopted in civil engineering area, especially in coastal and corrosive environments. Recent examples are fibre composite components to replace timber bridge components, lightweight decking and drop-in-place road bridges.

Composite solutions for traditional civil infrastructure applications, are often more expensive than traditional materials but do become competitive in corrosive environments or when weight or access is restricted. This weight advantage has been found to reduce transport and installation costs.

Recently, optical sensors are being placed on the outside of civil structures as a research endeavour and commercially in its infancy. These are to replace traditional sensors such as strain gauges. The embedding of sensors in fibre composites is still at an early stage and has manufacturing hurdles to cross before becoming a reliable method. These optical sensors have been found to be ideal for fibre composites due to their small size and ability to give several indicators of structural health at one time –such as strain, temperature, fatigue and damage.

The vacuum infusion manufacturing method has not been successfully used for embedding sensors commercially due to the vacuum pressure and handling damaging sensors during manufacture. Sensors require at least one inlet point on the component for the light source and reflected spectrum and this then becomes a point of sensor failure. A method for protecting the optical fibre from the manufacturing pressure and from being covered in resin is needed for the optical fibre to be accessed after curing. With higher performance products requiring oven post-curing, the protection method would need to withstand these temperatures.

This thesis seeks to develop the method of embedding a fibre optic sensor network using the vacuum infusion process for fibre composite. A sensor network will be designed to suit the loading of a bridge deck and bridge beam. After manufacture, these networks will be tested for accuracy.

1.2. Aims

- To develop, by experimentation, an efficient method for embedding optical fibre sensors in FRP structures. This will include techniques suitable for hand lamination and vacuum infusion manufacturing methods using glass and carbon fibre reinforcements. These same techniques can be extended to be used with resin transfer moulding, pre-impregnated fabrics and natural fibres.

- Investigate the suitability and performance of FBG sensors in FRP bridge structures. This would involve measuring in-situ health conditions, the ability to detect damage and sensor behaviour due to fatigue loading.

- To test and develop a prototype FBG based smart FRP bridge deck and a smart FRP bridge beam with SHM capabilities.

1.3. Outline of the report

Chapter 2 – Literature Review - a background about the composite industry and recent examples of FRP infrastructure is covered first. General information is given on the main fibre reinforcements and relevant polymer systems for structural applications. The theory for operating the new generation fibre optic sensors is presented along with recent examples of use in concrete and composite structures where the sensors have been embedded.

Chapter 3 - Experimentation and Analysis - sensor embedding techniques where experimentally improved to find efficient and reliable methods. Manufacture of a smart FRP bridge deck concept and smart FRP bridge beam concept is detailed with load testing and finite element analysis. Testing involved introducing damage, in the form of cracks for the deck and fatigue for the beam to investigate sensor response.

Chapter 4 – Data Analysis – covers the collection and manipulation of sensor data for strain and spectrum tracking conducted. Improved peak detection, spectrum distortions and the novel method of gradient spectrum symmetry is covered.

Chapter 5 -Results and Discussion – presents the results of the load tests including sensor data and spectrum indicators. The findings are discussed with the relevance to damage detection and structural health monitoring.

Chapter 6 – Conclusion - Finally, a conclusion is given that covers the implications of the findings and future work to be done.

2. LITERATURE REVIEW

2.1. Fibre Composites

Fibre composites are increasingly used in manufacturing for their high strength to weight ratios. They are typically made of a fibre with relatively high tensile properties and a matrix that provides good adhesion to the fibres. The combination of the two can result in properties that are otherwise not available in traditional materials. While traditionally used in the marine and aerospace industries, fibre composites are making inroads into the civil and mining industries.

Advantages of fibre composites are high strength to weight ratios (specific gravity =1.2~2.0), corrosion resistance, ability to manufacture complex shapes, ability to orient fibres in preferred direction and relatively inexpensive manufacturing equipment.

The methods of manufacture include hand layup, chopper gun spray up, resin transfer/vacuum infusion, prepreg and pultrusion, to name a few. Resin transfer, prepreg and pultrusion methods apply greater pressure during manufacture to result in higher fibre fraction ratios and higher mechanical properties. Where these methods are not possible hand layup and spray up processes are employed, which are more labour intensive. These manual methods rely on the skill of the operator and can result in slower production rates and quality issues. Components may also be post cured in ovens or microwave to achieve 'full strength'* ex-factory. (*more than 95%)

The methods of resin transfer and prepreg both consist of applying the reinforcements in layers and have great potential for embedding devices between layers during manufacture. For large structural components, resin transfer methods are far more cost effective than prepreg and so have been better utilised in infrastructure. The resin transfer method by vacuum, in this project, is made by layering the reinforcements in the mould and holding them in place with a small amount of adhesive. (Figure 2-1) An infusion medium layer is laid over the entire surface of the part with additional medium or channels placed for controlling of the resin flow. A vacuum bag is placed over the layers and sealed to the mould with sealant tape. Inlet and outlet ports are fitted and closed. The vacuum is attached to the outlet port and turned on at low pressure and the seal is checked. This pressure is increased gradually to the operating pressure while ensuring the bag is wrapping the component correctly. The resin is then mixed with its related catalyst/hardener and placed under the inlet port(s). An inlet port is opened inside the resin bucket and the resin is drawn through the mould. When the resin has fully passed the size of the component the inlet port is turned off but the vacuum is left on until the resin 'gels'. This is when the resin hardens to the point that it no longer requires the bag to hold it in place. The bag is then removed and the component is left to cure.

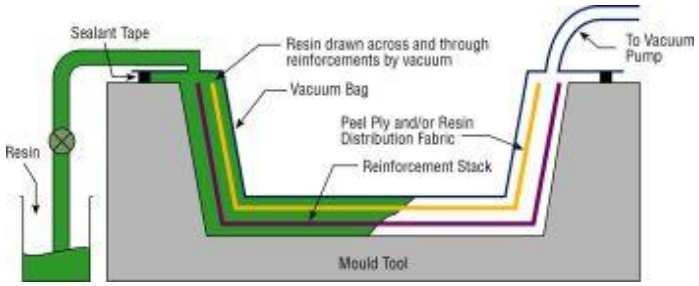

Figure 2-1: Vacuum Infusion or Vacuum Assisted Resin Transfer Process (Netcomposites, 2014)

There are a number of barriers in adopting fibre composites over traditional materials. There is a lack of understanding of the materials and a relatively short track record (used since 1950's) which has produced reluctance in engineers. Not having international or national composite material standards (Eurocomp is reference for designers) means design standards based on traditional materials are used and often disadvantage a composite solution. The failure mode that fibre composites exhibit is largely brittle and is difficult to detect signs of damage.

2.2. Overview of Composite industry –growing applications in civil infrastructure

The early development of advanced composite materials originated in the 60's with the new polymer/plastics production and the application of designer goods and furniture. Following the use of engineered fibres as reinforcements, such as glass and carbon fibre, the use in structural applications became possible. Firstly, FRP building block construction started in the 1970's along with load-bearing infill panels. These were primarily glass fibre reinforced polymer (GFRP) materials. The 1980's saw the use of FRP in off-shore structures. Rehabilitation and strengthening using FRP began in the early 1990's followed by the use of non-metallic rebar's for concrete reinforcement. Beyond the year 2000 has seen an increase in large structural units and monolith structures being built along with combinations of FRP with traditional materials (Hollaway, 2003). Of these structures, bridge applications make up a large proportion.

FRP bridges have been in use since the 1980's, with the first FRP road bridge being opened in 1994 –the Bonds Mill Bridge in the UK. Since then, bridges have been built with FRP in combination with other materials, like the Wickwire Run Bridge USA (1997), which has steel beams and GFRP pultruded decking units. Also some all-composite bridges have been built, such as the ASSET Highway Bridge, UK (2002) and the Hardgrave Rd Highway Bridge, Australia (2014). Both of these have design capacities in excess of 40t (or SM1600 loading according to AS5100). Recent examples of these solutions, seen in Figure 2-2, are two highway bridge solutions built by BAC Technologies, in Australia, that answer the problem of ageing timber infrastructure.

Figure 2-2: FRP Highway Bridge Structures: a) Components for Timber replacement (2013) and b) Monolith Highway Bridge Deck (2014)

The bridge components (Figure 2-2a) were designed to match the flexural and strength properties of new F27 hardwood in keeping with the size of the existing timber components. The monolith bridge structure is an example of where a new structure can be designed for structural efficiency and optimised production costs.

2.3. FRP Infrastructure Design Approach

There are two clear approaches to designing FRP infrastructure, as presented by Nelson (2014). One approach is to design and construct FRP structural components 'like-for-like' as a substitute for the traditional materials. This means matching flexural properties of the sections and ensuring strength capacities are exceeded while keeping the geometric design relatively unchanged. The end result is a product that looks very much like the alternative –for example an FRP 'I' beam instead of a steel 'I' beam. The bridge piles, headstocks and bracing in Figure 2-2a are an example of this approach. The other approach is to optimise the design utilising the high strength to weight ratio but relatively low E modulus of the FRP that results in quite different designs for structural efficiency. These often lend themselves to combining components into a single dual purpose component or even a monolith structure. The example of the FRP highway bridge in Figure 2-2b is of a deck and five beam structure with internal bracing that was made largely in one resin infusion process. This design was optimised to meet the SM1600 highway loads and L/600 deflection limit for Australia.

While large and high capacity structures are clearly possible, most of the implementation of these advanced materials has been in low capacity applications, such as boardwalks and pedestrian bridges or as a strengthening method. Figure 2-3 shows an example of an FRP pedestrian bridge that was chosen specifically for the material's weight saving and corrosive resistant properties.

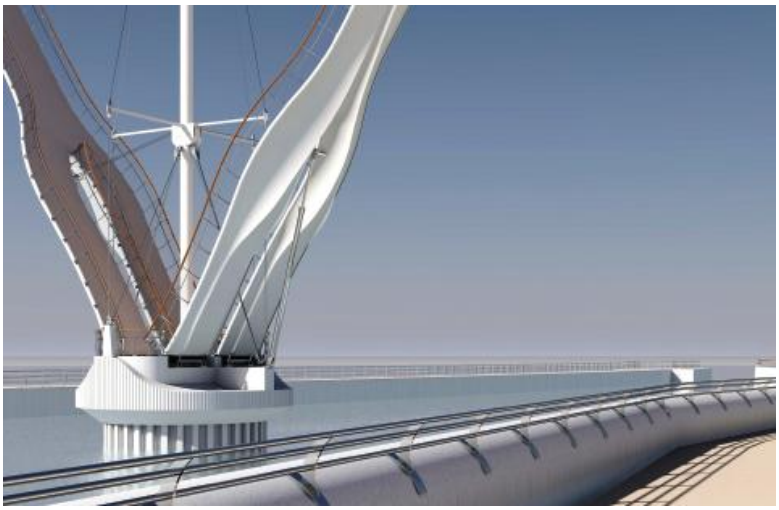

Figure 2-3: Rhyl Harbour Bridge, Wales (Gurit, 2013)

It consists of two mirroring, 30 metre long decks, which are hinged on a central caisson and lifted by cables running up to a central mast, almost 50 metres tall. The construction was based on a GFRP and foam sandwich structure with carbon fibre stiffening in the beams. It was manufactured by Gurit - UK in 2013 who did extensive computer analysis for design optimisation. Special attention was given to modal (natural frequency) analysis which is of concern in pedestrian bridges. Gurit have begun validation of the design natural frequency and deflections with a temporary SHM system. Here it can be seen that FRP materials also offer engineers and architects flexibility in design to incorporate curves and aerodynamics resulting in striking landmarks that are also efficient.

For FRP composite materials to be further utilised in civil infrastructure, a better understanding of the materials and long term behaviour is required.

2.4. Fibre Composite Material Properties

FRP structural materials are made of high strength fibres in a polymer binder, or matrix. They derive their tensile and bending properties largely from the fibre type and orientation, which are predominantly E-glass or Carbon fibre. This is due to the volume fraction of the fibres, V_f, constituting between 50-75% of the overall material in high quality FRP.

A bulk material, such as a metal or polymer, is isotropic in behaviour (Figure 2-4a). Meaning it has the same properties in all directions. This can be represented by the following relationship between the Young's modulus of the material in the *x, y*, and *z* directions:

$$E_x = E_y = E_z \qquad \text{Eq. (1)}$$

The same goes for the material's tensile, shear, electrical and thermal properties. This is relevant since the matrix in FRP is a polymer and behaves this way.

If we consider a single layer of FRP (a ply) with fibres only in one direction (Figure 2-4b), also called unidirectional, it is found that it has different mechanical properties in all directions. This is described as an orthotropic material and can be represented by the following for the *E* modulus:

$$E_x \neq E_y \neq E_z \qquad \text{Eq. (2)}$$

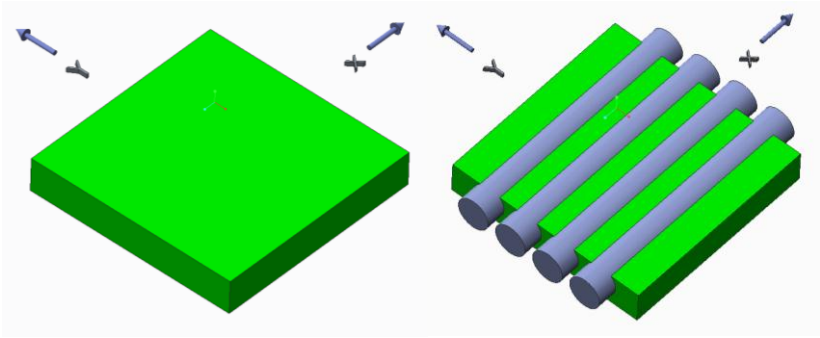

Figure 2-4: Determining Mechanical Properties of FRP: a) Polymer Isotropic Materials, b) FRP Orthotropic Materials

The convention in notation is referring to the 11 direction or x axis as the components major axial direction which is often the direction of the majority of the fibres. The mechanical properties in this direction are typically the greatest.

Determining the property of an FRP material theoretically can be found from its constituents by applying the rule of mixtures for each direction. This rule is applied dependant on the fibre direction. To calculate mechanical properties in the fibre direction, the formula takes on this form:

$$E_c = V_f E_f + V_m E_m \qquad \textbf{Eq. (3)}$$

Where E_c=elastic modulus of the composite, E_f=elastic modulus of the fibres, E_m=elastic modulus of the matrix, V_f=volume fraction of the fibre, V_m=volume fraction of the matrix. The elastic modulus of the composite E_c with be the sum of the products of the elastic modulus and volume fraction of each constituent, in the fibre direction. This rule of mixtures can be applied to other mechanical properties, such as tensile strength and shear strength for this axis.

$$\sigma_c = V_f \sigma_f + V_m \sigma_m \qquad \textbf{Eq. (4)}$$

Where σ_c=tensile strength of the composite, σ_f =tensile strength of the fibres, and σ_m=tensile strength of the matrix.

$$\tau_c = V_f \tau_f + V_m \tau_m \qquad \textbf{Eq. (5)}$$

Where τ_c=shear strength of the composite, τ_f =shear strength of the fibres, and τ_m=shear strength of the matrix.

For properties perpendicular to the fibre direction, in the y axis, the rule becomes the inverse of the sum of the ratios of the volume fraction and the mechanical property:

$$1/E_c = 1/(V_f E_f + V_m E_m) \qquad \textbf{Eq. (6)}$$

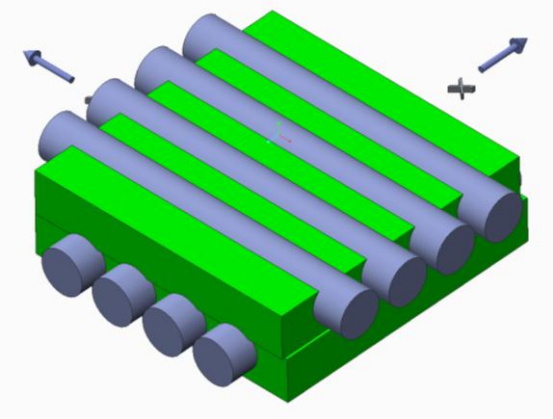

Figure 2-5: Quasi-isotropic Material

A quasi-isotropic material can be produced, having the same properties in different directions, by placing successive layers with fibre directions evenly alternating (Figure 2-5). This greatly reduces time for design analysis and has been found to increase fatigue and damage resistance.

$$E_x = E_y \approx E_z \qquad \text{Eq. (7)}$$

While these formulas are a good estimation when FRP properties are not known, they have a tendency of over estimating properties. These calculations assume a perfect bond between the fibres and matrix –which is not reflected in reality. Some designers have a practice of using a reduction factor (0.8 to 0.9), but it is recommended that mechanical properties be determined by mechanical testing of sample laminates. (Campbell, 2010)

These fibres have higher tensile strengths than mild steel but suffer from a comparably lower *E* modulus. According to Bunsell and Renard (2005) glass fibre reinforced polymer (GFRP) contributes to 90% of the world's FRP market. This is largely due to the relatively cheaper cost of the material. As can be seen in Table 2-1, glass fibre has a specific gravity (density ratio compared to water) of 2.5 and the carbon has a specific gravity of 1.8. To find the specific modulus, the E modulus is divided by the specific gravity. The specific modulus of glass fibre is 27, which is roughly one sixth that of carbon fibre at 164. However, carbon fibre can be more than nine times as expensive per kilogram as the glass fibre, resulting in the glass often being the more efficient choice.

Table 2-1: Comparison of Reinforcement Materials for Composites (Bunsell and Renard, 2005)

Materials	Specific Gravity (kg/m^3)	Young's Modulus (GPa)	Specific Modulus (GPa)
Steel	7.9	200	25.3
Titanium	4.5	116	25.7
Glass fibre	2.5	72	27.6
Aluminium	2.7	76	28
Kevlar 49 fibre	1.45	135	93
Carbon fibre	1.8	295	164
Carbon (ultra-high modulus fibre)	2.16	830	384

Structural components tend to be made of many long continuous fibres that are built up in layers (lamina). The result is a layer with extremely high properties in the fibre direction since the fibre is in tension. Relatively low properties are found perpendicular to the fibre direction because the fibre is in shear. Each layer may then have differing orientations to cause the finished product to have adequate strength and flexural properties in the direction that it is required.

The structural health, short and long term, of FRP materials relies on the ability of the fibre to transfer the load to the polymer matrix through the fibre-matrix bond. This bond has been found to be greatest in thermosetting, cross-linking polymers: specifically the vinyl-esters, the epoxies and the polyesters. With polyester having lower mechanical properties and a tendency for water absorption, it is less appropriate for these structural applications. Epoxy is well known for its superior bond strength to various materials and is utilised in many structural products, such as grouts, adhesives and FRP. Vinyl-ester (VE) has the best corrosive resistance of the three, comparably good strength and is significantly less expensive than epoxy so is becoming more widely used as the polymer in FRP structures.

Failure under continuous loading starts by way of micro-cracks in the matrix that are invisible to the naked eye (at around 1% strain for polymer matrixes) which weaken the bond between layers. As the cracks increase in size, delamination begins to occur and fibres under the highest loads then fail. (Marshall et al. 2003) These areas of early cracks can be detected by more accurate methods than visual inspection which are part of structural health monitoring.

Some of the long term performance of FRP has been researched but is not fully understood and there is concern over the degradation and fatigue of the material where visual inspection is difficult.

2.5. Structural Health Monitoring (SHM)

SHM is the monitoring of the structure, using non-destructive evaluation techniques (NDE) to improve the reliability and safety of a structure as well as to reduce the long term maintenance costs. The goal is to integrate sensing and possibly actuation devices to record, analyse and possibly predict the loading and damage conditions of a structure (Boller and Meyendorf, 2008). In this way, early detection of damage can be possible long before traditional visual inspection would have noticed any problem.

The sensors used in SHM include: strain gauges, piezoelectric, micro-electromechanical systems (MEMS) and fibre optic sensors. Among these, the fibre optic sensors have been of most interest for embedding in composites because they share some characteristics with FRP. The locations where FRP are utilised tend to be aggressive or corrosive environments that would deteriorate electrically based sensors. This will be discussed further later. Traditional strain gauges, piezoelectric and MEMS are all electrically based and require electrical wiring, and a power supply voltage in close proximity. Fibre optics, however, can supply a light wave from a source that is far away along a fibre optic cable.

While structural designers have done their due diligence, with the knowledge they have at the time, several examples of unexpected behaviour and even failure can be seen in the resonance of bridges. The Millennium Bridge in

London, a 325m steel suspension pedestrian bridge completed in 1998, experienced unexpected lateral movements as a response to the foot traffic, described as 'rocking' or 'swaying', and was closed temporarily while additional stiffening and dampening was installed. (Fitzpatrick, 2001)

In past cases, natural resonance has been explained for the collapse of a number of bridges causing loss of life, namely: Broughton Suspension Bridge, England 1831, Angers Bridge, France 1850, and the Tacoma Narrows Bridge, America 1940.

2.6. SHM of Composite Structures

FRP structures can benefit from SHM to validate the residual life of the structure and be an early warning sign of damage.

Keulen et al (2011) has recently successfully embedded FBG sensors using the resin transfer method. The steel moulds required a number of modifications including holes drilled and stainless steel tubes at the ingress/egress locations of the optical fibre. In testing, only tensile loads in the direction of the sensor were performed which, of course, had good correlation. Complex component geometry or components that undergo multi-axial loading were not discussed.

Nakamura (2011) successfully inversely determined distributed loads from FBG strain data for an idealised aircraft wing. The assumption made is that the stresses on the component occur primarily due to the distributed load and are in one axis.

The desire for SHM of FRP structures has grown along with the increased use of FRP decking for higher load applications, such as road bridges. These kinds of critical infrastructure have enormous impacts on the community if they were to be damaged or fail. FRP bridges have been in use since the 1980's, which is a relatively short time to create significant data needed. Civil infrastructure routinely has serviceable life expectancy in excess of 100 years which highlights the need for providing innovative FRP structural components with embedded SHM.

2.7. FBG Theory and measurements

Recent developments in sensor technology have made it possible to place micro-scale fibre optic sensors within the FRP material during manufacture that does not affect the material properties or design of the structure. Among these, Fibre Bragg Grating (FBG) sensors have been found to be superior for SHM of FRP materials since they are immune to electromagnetic fields, non-corrosive, have the ability to be multiplexed and can carry signals very long distances (up to 5kms). Recent research has looked at ways to increase the transmission distance to beyond 20km (Kim et al, 2012) for remote location sensing.

FBG sensors are fabricated in the core region of specially fabricated single mode low-loss germanium doped silicate optical fibres. The optic fibres have diameters in the range 50~250um. The grating is a laser-inscribed region which has a periodically varying refractive index. This region reflects only a narrow band of light corresponding to the Bragg wavelength λ_B, which is related to the grating period Λ. (Kashyap, 1999) Common FBG wavelengths are in the range of 500~1600nm.

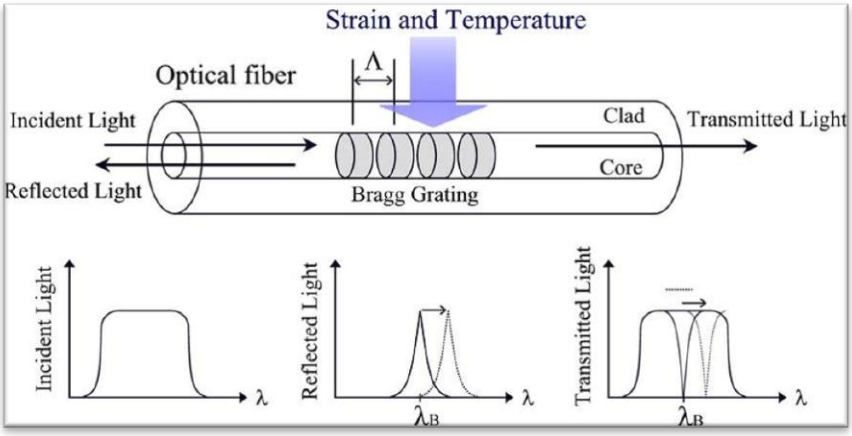

Figure 2-6: FBG Sensor Optical Measurement

Measurements are essentially taken by wavelength scanning. Light is sent through the optical fibre, most is transmitted through the grating and the rest is reflected (Figure 2-6). The wavelength reflected in an FBG sensor is proportional to the grating size, obeying the following relationship:

$$\lambda_B = 2n\Lambda \qquad \textbf{Eq. (8)}$$

Where λ is the back reflected Bragg wavelength, n is the average refractive index of the core and Λ is the spacing between the gratings. When an FBG undergoes strain in the axial direction the gratings increase in size and in turn light is reflected with a higher wavelength. This change can be detected by a change in reflected wavelength at the spectrum peak reading. The change in peak wavelength is linearly proportional to the strain in the sensor and is so can be used as a reliable strain sensor. Due to the change in applied strain $\Delta\varepsilon$, and temperature change ΔT, there is a change in the wavelength, $\Delta\lambda_B$ according to the following equation:

$$\frac{\Delta\lambda_B}{\lambda_B} = (\alpha_f + P_t)\Delta T + P_e\Delta\varepsilon \qquad \textbf{Eq. (9)}$$

where α is the coefficient of thermal expansion of the optic fibre, P_t is the thermal-optic coefficient and P_e is the strain-optic coefficient, which are all available from the manufacturer. Under an isothermal condition (constant temperature) the resulting strain can be determined by simplifying and rearranging equation 9 to form equation 10:

$$\Delta\varepsilon = \frac{\Delta\lambda_B}{\lambda_B}\frac{1}{P_e} \qquad \textbf{Eq. (10)}$$

So the strain within the layer of the FRP can be determined by placing an FBG sensor within that layer during manufacture. Degradation in the material can be found by the strain increase over time under the same loading.

Other sensor measurements other than strain and temperature have been possible from the development of FBG based load cells, tilt sensors, accelerometers, displacement transducers and pressure sensors. (Cusano, et al, 2011) These utilise a casing or simple mechanical device to convert the target measurements back to strain in the sensor –much like has been done with traditional strain gauges in the past.

Recently, research has been in the area of obtaining more information from the full reflected spectrum of FBG sensors and not just the peaks. It is observed that changes to the spectrum shape occur when the FBG sensor itself undergoes bending, torsion or if there is a non-uniform strain distribution over the length of the sensor (Hill and Edgerton, 1994). These changes in the spectrum can be described as a distorted or chirped signal, as shown in Figure 2-7.

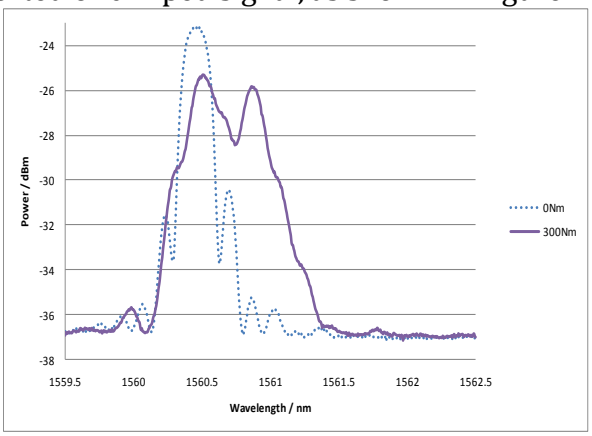

Figure 2-7: Normal and Distorted FBG Spectrum Signal

Changes in the spectrum have been analysed to find localised compression of the fibre (Hill and Edgerton, 1994), to monitor delamination growth in FRP (Takeda et al, 2008) to indicate fatigue (Epaarachchi et al, 2009) and damage detection.

These have primarily used the Full Width at Half Maximum (FWHM) of the spectrum to indicate distortions. The FWHM generally increases as the signal becomes more distorted. A distortion index, proposed by Kahandawa (2012) which is the value of the FWHM/Power Range ratio and is tracked for changes over time, has shown promise in indicating torsion or micro-bending in the sensor. It was shown clearly that this distortion index increased over time with fatigue since the spectrum became wider with fatigue. To ensure that this distortion index is indicating fatigue, the sensor needed to be installed without chance of compression or bending of the sensor. Some encapsulation techniques have been successful in reducing these false positives and these include casting the sensor in an epoxy resin based block or laminating the sensor between layers of FRP, both of which are then fixed to the structural member by bolt and or glue. The large surface area of the bond between the sensor package and the structure ensures measurement accuracy and sensor robustness.

2.8. Embedding FBG

In the case of new FRP and concrete structures, these sensors can be positioned within the structural components during manufacture and can result in measurements from within the structure that would otherwise not be possible with conventional sensors. The sensor packets (blocks, tubes or plates) used in surface mounting are still required in concrete structures as the manufacture process imposes large forces on the sensors. For FRP structures, these packets are no longer needed as the sensor is placed in between the layers during manufacture (Takeda, 2011).

It is only in recent years that FBG sensors have been embedded within materials and this has tended to be on large structures and in corrosive/volatile

environments like on bridges and offshore platforms. The largest of these would be the Dongying Yellow River Bridge in Shandong, China, 2743m long, 26m wide with its largest span of 220m. Over 1800 FBG sensors were installed during manufacture for monitoring strain and temperature in the concrete. Other uses have been in monitoring cable stays, reinforcements and repairs. The embedding capability of FBG's means they can be placed in otherwise unreachable locations and be protected from damage.

Rodrigues et al (2010) successfully installed FBG sensors in steel casings that where then cast into the concrete beams of a bridge. The steel casings where prepared with riflings to aid in bonding with the sensor and placed in the mould before casting the concrete beams. The steel casings cause the small sensor to measure the average strain over the length of the casing and eliminate sensitivity to localised strain. The use has extended to monitoring the FRP strengthening of concrete beams (Sarazin and Newhook, 2006) and now the monitoring of FRP structural components in aircraft (Epaarachchi et al, 2009).

By utilising a fibre optic sensor network that is inside the FRP decking panel, a smart deck is produced. Once the deck panel is installed in the bridge, SHM can be done by connecting the optical data acquisition to the smart deck itself.

2.9. Summary

The past literature has shown that embedding an FBG sensor network in an FRP structure has great benefit to the monitoring of the structures health and possibility for damage and fatigue detection. It has been found that the embedding methods require some development along with the analysis techniques.

3. EXPERIMENTATION & ANALYSIS

3.1. Introduction

Three main issues are addressed in this chapter: Sensor embedding techniques; Smart FRP Bridge Deck development and Smart FRP Bridge Beam development.

3.2. Experimentation of Sensor Embedding Methods in FRP

Methods of embedding sensors in FRP are not well described in the literature and pose a real hurdle to the implementation of this technology. A number of methods were experimentally trialled to compare the reliability and feasibility of each method. When talking about embedding methods, they can be broken into three categories: sensor placement and securing, passing through FRP layers and ingress/egress treatment. While the first category of placement and securing has been successfully done in laboratory settings, the securing of sensors during manufacture in a factory setting requires more thought and a more robust solution. The ability to pass through fabric layers to the desired location is essential for accurate measurement to take place and this has been found to be a time consuming part of the fabrication that needs to be addressed. The ingress/egress location and treatment of the optical fibre is critical to its long term use and this has shown to be the most likely location of sensor damage to occur due to rough handling. The major concern is that the sensor can be accurately located, survive the manufacturing processes and have long term protection during service. All of this needs to be achieved by efficient embedding techniques that are suited to manual methods (hand lamination) and pressurised methods (resin transfer methods).

3.3. Sensor placement and Securing

The methods for placement trialled were: hand threading the optic fibre; using various adhesive tapes to hold the fibre in place either on the fabric or to the mould; use of a spray adhesive or resin to attach the fibre to the glass fabric layers; and using silicon rubber as an adhesive. Simply threading the fibre did not result in enough friction to hold the sensor in place and it easily was moved by accident. Using adhesive tapes worked when attaching to the mould but if attaching to the fabrics would result in tape being included into the finished product which is not ideal. The spray aerosol adhesive trialled (3M Scotchweld Super 77) was very good at holding the sensor in place but it was found that using it excessively caused a dry area that the resin didn't adhere to during wet-out. A fast drying silicon rubber was also used as an adhesive to bond the optic fibre to the fabric, but not at the FBG sensor location. This method required longer drying times (more than 30 minutes) and caused greater resistance to the resin system during wet-out. The end result was a panel with defects that should be rejected. The last method of using the same resin system of the panel to adhere the sensor produced the most defect free panel with hand lamination but did require an additional 30 minutes of curing. This method showed problems during infusion when too much resin adhesive was used the resin flow was affected.

3.4. Placing Sensor in Fabric Layers

To position sensors accurately between FRP layers a number of methods were tested. These included placing the entire optic fibre between two layers

during lay-up (Figure 3-1); threading the optic fibre through layers after placing those fabric layers; using a curved needle for threading into and out of fabric layers and using a small tube to temporarily thread the optic fibre through which is then removed.

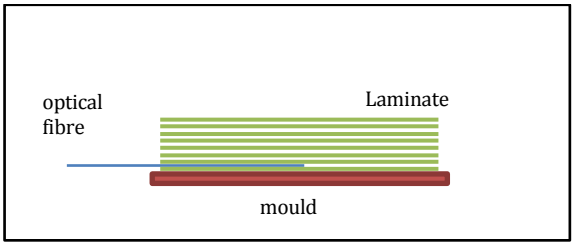

Figure 3-1: Method of Embedding Fibre Optics with Hand Layup

Placing the FBG sensor between layers posed little problem except that it only allowed the ingress/egress point to also be in that layer, which is not always desirable. There is usually an exterior surface layer that requires monitoring while the sensor ingress/egress is better on an underside or in a protected region. Threading the optic fibre alone is quite tedious and difficult to see against the glass fabric. Trying to bend it to return to an egress point was also difficult and time consuming. This led to the use of a curved needle or wire to then slide on a small tube. After removing the wire, the optical fibre is threaded through the tube into position. The tube is then removed to leave only the optic fibre threaded through the fabric. This method proved to be very fast and accurate. It also made it possible to be more flexible in the positioning of the sensors –whether in layer and ingress/egress locations.

3.5. Ingress/Egress Treatment

In the process of handling, it became clear that the ingress/egress locations were the most common reason for sensor damage and needed to be investigated. The possible methods tested involved protecting the exposed optic fibre: in resin or silicon rubber; sliding on a small tube; covering it with tape; or coiling the fibre in a silicon-based bag.

Coating the optic fibre in resin proved to be a mistake since it now made the fibre more brittle and prone to damage. The silicon, however, did just the opposite, and made the fibre more resilient. The silicon resisted resin being attached to the optical fibre and could be removed later to access the fibre, if needed. Care needed to be taken in close proximity to the surface of the FRP as the silicon was known to cause surface defects. Sliding on a small tube was beneficial to hold the excess cable in position but since it easily filled with resin, injecting silicon in it was tested. This required a much longer cure time (hours) since only the ends were exposed to the air. The tube did have some use in vacuum infusion when running the optic cable outside the infusion bag. Covering the cables with tape was difficult and the adhesives on the tapes appeared to have a small reaction with the resin system which could lead to product defects. Lastly, a silicon-based plastic bag, made from infusion bagging material was used to coil the optical fibre inside. It was sealed with high-tack tape some were filled with silicon rubber. This method was time consuming but did protect the cables well. There was some movement of these bags during handling so some were taped down. The adhesive in the tape reacted slightly with the resin, as stated before. During the infusion test, the bags compressed on the test panel which affected the

resin flow and created slightly dryer areas. One silicon bag leaked silicon rubber which wasn't fully cured that resisted resin to wet-out an area. Overall, protecting the optical fibre with the bag was not successful. The best method was to coat the fibre in silicon rubber, being careful not to contaminate the fabric and wait until it fully cured before applying the resin. This method was also the best for vacuum infusion and the result is in Figure 3-2.

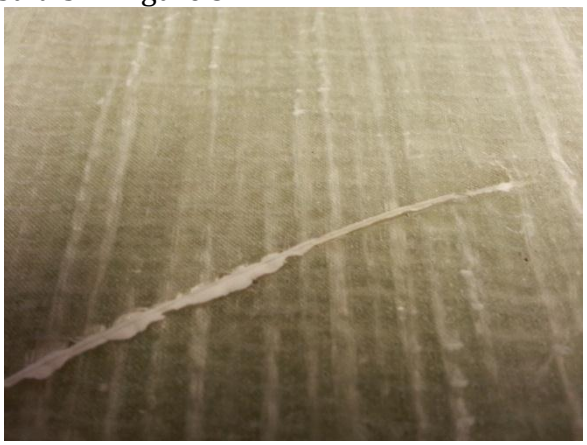

Figure 3-2: Silicon Doping of Optical Fibre at Ingress

3.6. Vacuum Infusion Sensor Embedding Method

Secondly, a prototype decking panel was produced using vacuum infusion. Four layers of 600gsm biaxial glass fibre mats were laid over peel ply. The optical fibres where weaved between the third and fourth layer by way of a Ø0.2mm bent wire followed by a Ø1mm smooth plastic sleeve (Figure 3-3). The fibre is then passed through the sleeve and the sleeve is removed to leave only the optic fibre in place. Silicone rubber is coated on the exposed section of fibre and allowed to cure to resist resin adhesion to the optical fibre. Peel ply, infusion mediums and vacuum bags where then be applied in the usual manner.

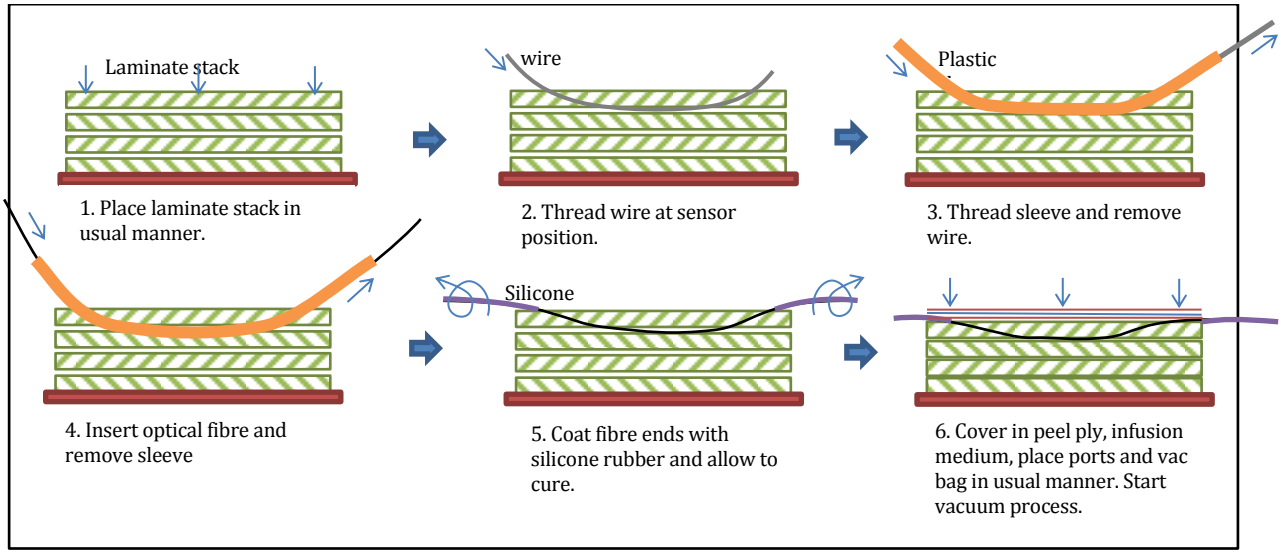

Figure 3-3: Method of Embedding Fibre Optics with Vacuum Infusion

The process added approximately 1hr of additional production time to embed four sensors (Figure 3-4). The vacuum was ramped to 90kPa and held for 1hr. Infusion was conducted with vinyl ester resin 6037(infusion grade) with 2% Norox MEKP catalyst at 75kPa @22^{o}C. Once fully wet out, the pressure was raised to 90kPa and held for 8 hours while curing at ambient temperature.

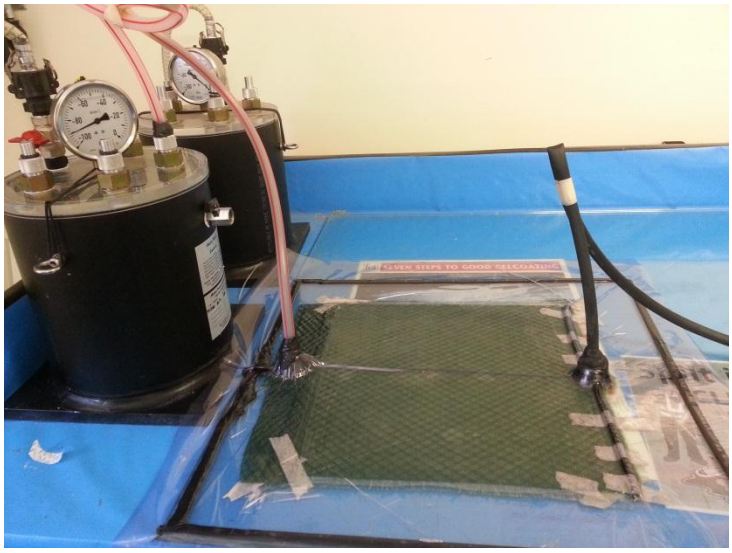

Figure 3-4: Test Panel made by Vacuum Infusion

3.7. FRP Deck Concept with Embedded FBG

A sensor network for a smart deck will need to detect the UDL and concentrated loads for a given span based on the typical bridge loading presented earlier. A sensor network was designed to be capable of detecting loads from multiple directions and in several load cases. The network consists of six FBG sensors in a rosette pattern –oriented at 0, 180, +90, -90, +45 and -45 degrees. The sensors were labelled 00-1, 00-2, 90-1, 90-2, 45-1, 45-2 respectively (Figure 3-5). The sensors were placed 20mm from a central point of the loading for an expected improved load detection. The sensors used were 125µm diameter with a central wavelength in the 1550nm range. A single ingress point was chosen to simulate a product where access is limited or where the sensors are multiplexed and a single connector is required. At the bends in the fibres, a minimum bend radius of 50mm was maintained to ensure a good signal to noise ratio and to reduce the chance of breakage. New standards recommend 1 inch and 2 inch bend radii for unloaded and lightly loaded optical cables respectively. (ANSI/TIA/EIA-568B.3, "Optical Fiber Cabling Components Standard").

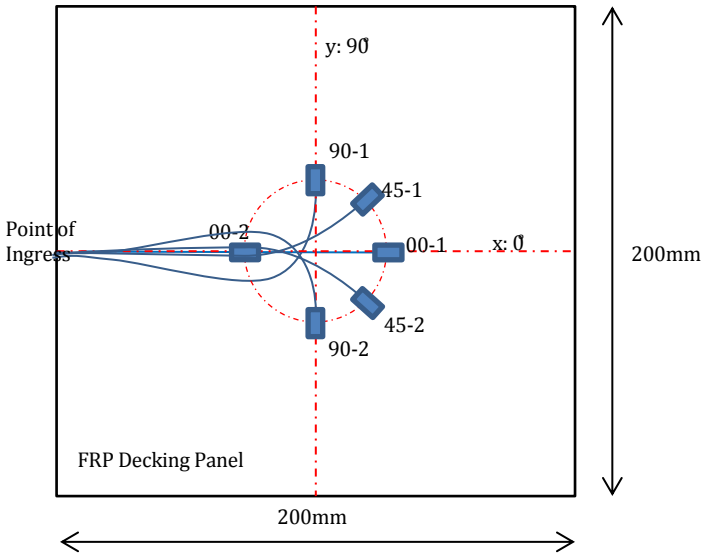

Figure 3-5: FBG Rosette Pattern with a single ingress point.

From the experimentation, issues relating to applying embedded FBG's to a larger bridge structure will be worked through, since the size and loading of an actual bridge deck has been scaled. It is anticipated that a smaller number of sensors will be satisfactory, when the improved embedding techniques are validated.

3.8. Finite Element Analysis (FEA) of Deck

Finite element analysis of the deck panel was conducted to confirm hand calculations and simulate damage. The panel (200x200x4mm) was modelled using Strand7 with 12545 nodes and 4096 quad elements as a laminate of 8 ply of 0.5mm thickness each (Figure 3-6).

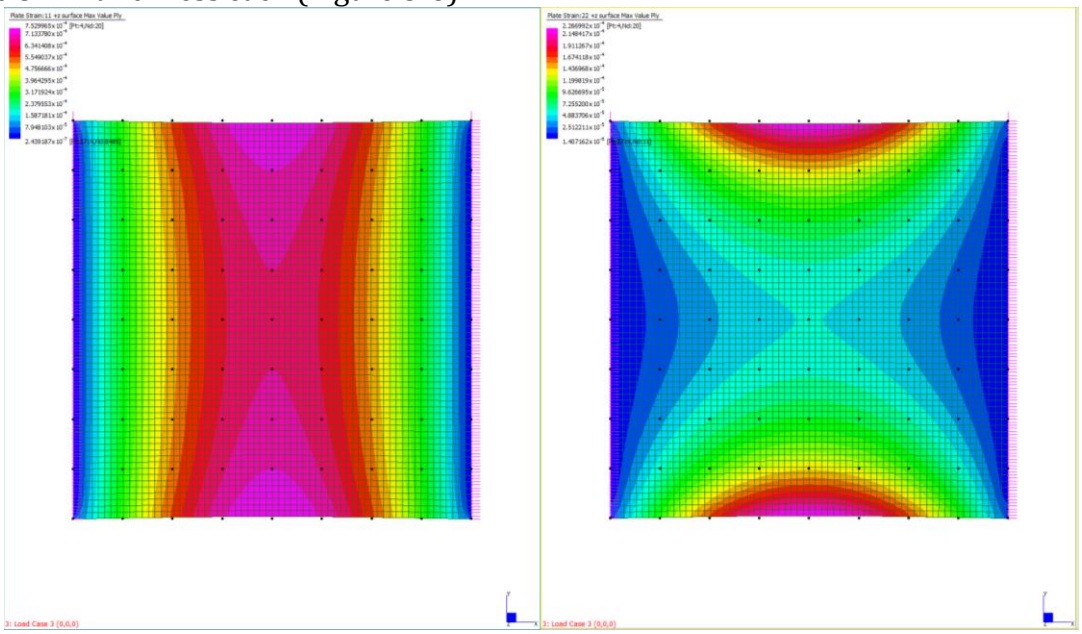

Figure 3-6: Strain Distribution under UDL: a) xx b) yy

The FRP panel was simply supported with a uniformly distributed load of 2.453kPa which is equivalent to a 10kg load equally distributed. The expected

maximum strain found in the panel in the x direction was $753x10^{-6}$ strain on the lower face at the unsupported edge. In the y direction the maximum strain was predicted to be $227x10^{-6}$ at the same edge. The predicted strain values were tabulated for each sensor location for later comparison with the load tests.

3.9. Deck Load Testing

Load tests were conducted at low stress (<$1x10^{-3}$ strain) to ensure damage did not occur to the panel during the first stage of tests. A bridge deck panel was simulated as a simply supported panel under uniformly distributed loading (Figure 3-7). The loads applied were from 1kg to 10kg in 1kg increments corresponding to a UDL of 2.453kPa over the 200x200mm area. Strain readings and full spectrum data was collected for each sensor under each load.

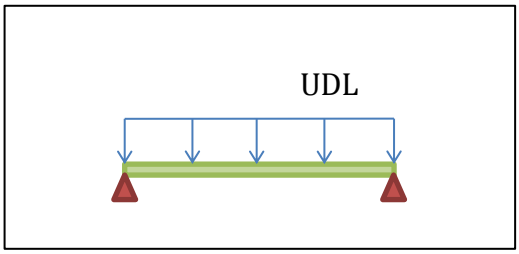

Figure 3-7: Simply Supported Load Test Configuration

A compression test was done for a UDL for the same range of 0 to 2.453kPa on a fully supported panel since distortions in the reflected spectrum is known to be caused by compression and combined loads in the sensor (Figure 3-8). In this test the panel was unable to bend on a fully supported test bench so the effect of compression (out of plane to the fibre direction) could be determined. The strain and full spectrum data was collected for each sensor.

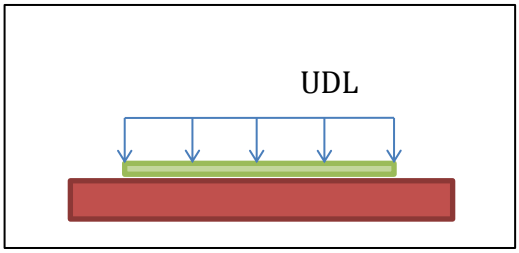

Figure 3-8: Compression Test Configuration

3.10. Optical Signal Processing

The data collected was in the form of a text file with 16000 signal values (in decibels) over a wavelength range for each load. A simple program was developed using Matlab to read these data files in order, simplify the data and plot the key information for interpretation by the operator.

The reflected spectrum showed distinct peaks with a fairly consistent shape throughout the loading. The top of the peaks showed some noise that was treated by applying a seven point average function to smooth the data. Minor peaks indicated distortions existing in the sensor due to sensor manufacture and possibly uneven curing rates in the FRP.

Due to possible fluctuations in the power transmitted through equipment which in turn causes fluctuations in the power (dB) reflected, it was important to normalise the power range for clear comparison. The spectrum was normalised

to values between 0 and 1 by subtracting the minimum power and dividing by the power range for each sensor (Figure 3-9). To reduce data points the wavelength range was clipped at a nominal +/-5nm from the manufacturer's specified wavelength –this is three times the range expected in the testing.

To aid in tracking the peaks and spectrum distortions, indicator points where chosen at the spectrum peak, 95%, 70% and 50% of maximum. The spectrum widths (nm) were calculated at these points 95%, 70% and 50%. The width at 50% is also known as full width at half maximum (FWHM). Much larger distortions and noise are found in the reflected spectrums below the 50% power range and so a spectrum indicator in this region was not seen to be of great value.

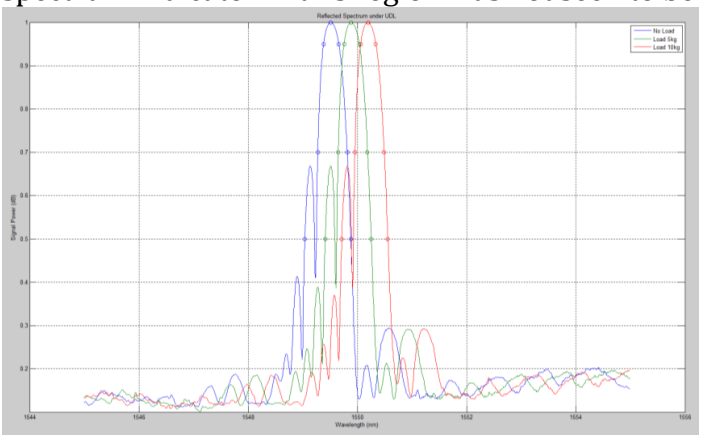

Figure 3-9: Normalised Spectrum with Spectrum Indicators at 50%, 70%, 95% of maximum.

The spectrum indicators are proposed to be a simplified method for tracking changes in the spectrum and therefore find better indications of damage. Peak detection was also trialled using the mid wavelength of the two 95% data points since little distortion is found in this region. A midpoint wavelength is found between the two points as an estimated peak wavelength. The corresponding strain was calculated and compared with the peak data and the FEA prediction.

3.11. Damage Detection in FRP Bridge Decking using FBG Sensors

Cracks were then simulated by milling a 1mm wide notch in the top surface of the panel with a CNC router with a 'v' cutter. These notches where increased to lengths of 2, 5, 10, 15, 20mm between UDL tests to simulate crack propagation. The effect on the spectrum response was recorded and processed for analysis. These simulated cracks where conducted at two locations: one centre span and one closer to the support.

The strain concentrations were simulated with FEA (Strand7) with the strain contour plots shown in Figure 3-10.

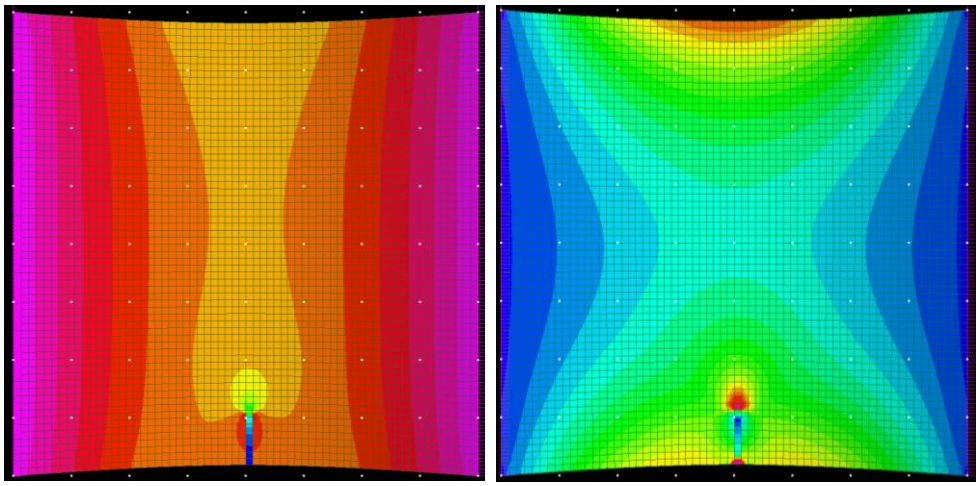

Figure 3-10: Strain Contour due to small notch determined by FEA: a) xx (across), b) yy (up).

It should be noted that the strain distribution found in the 0^o (xx) direction appears to increase strains in very close proximity to the damage whereas the strain field in the 90^o direction appears to affect a larger region but with less effect. This leads to the obvious conclusion that the closer the strain sensor is to the damage the better it will be at detecting damage early. Both sensors in the 0^o direction and the 90^o direction show concentrations in their readings but due to the saddle back topography the strain concentration in the 90^o direction is larger. This does not necessarily mean placing a sensor in this direction is better because the strain readings in this direction are very small so the detection in changes in strain will be less accurate. Placing a sensor in relation to future damage is not always possible since damage may occur in practice in locations that are not as predicted. For regular strain measurement of the deck panel and general SHM, the sensors parallel to the bending will show signs of excessive strain which indicate reduction in performance.

In order to compare the damage distance of several sensors, an additional sensor was placed on the surface of the underside of the panel 25mm from the edge and parallel to the edge. This additional sensor was labelled 00-3 and is indicated in Figure 3-11.

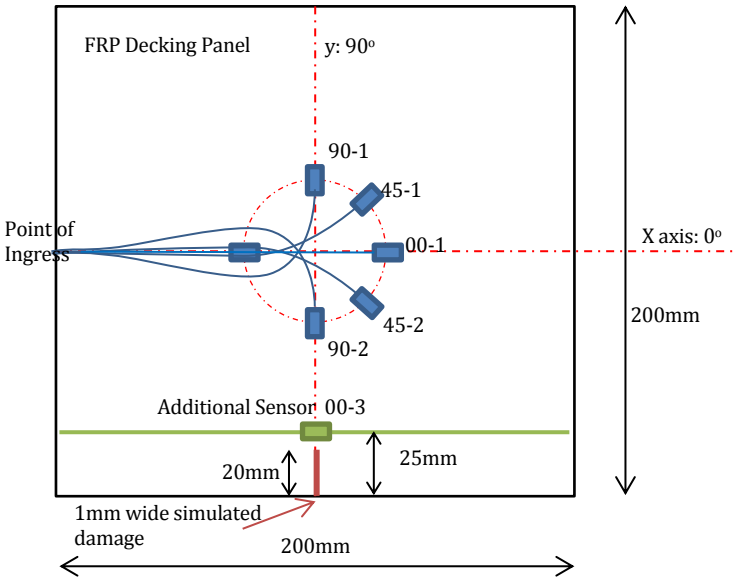

Figure 3-11: Simulated Damage in Model Deck

The load tests were conducted as before –a simply supported UDL in the range of 0 to 2.453kPa - as the notch was progressively increased in size. The strain values and full spectrum data were recorded for comparison with the undamaged deck panel. The spectrum shape factor and distortion indexes where used to track the changes in the signal spectrum of all the sensors.

3.12. Hybrid FRP Beam Concept with Embedded FBG

A 1m span scale model beam was designed for manufacture using vacuum infusion with embedded fibre optics to demonstrate the embedding method in a more complex part and to test the FBG sensors resistance to fatigue loading. Once this was established, the loading was incrementally increased with further cyclical loading to determine the sensors' ability to detect fatigue in the beam.

3.13. Hybrid FRP Beam Design

The beam was designed to have strength and flexural properties that are indicative of a bridge beam. It would span 1m with a service load of 2kN and meet an L/300 deflection limit. The materials chosen were biaxial E-glass (XE $0^0/90^0$) and unidirectional carbon (UC 0^0) fibres in an epoxy-vinyl ester (VE) matrix which are commonly used materials for structural FRP. As seen in Figure 3-12, the construction consists of a lightweight core of 35kg/m^3 polyurethane foam, 1mm thick UC flanges, top and bottom, surrounded by 2mm thick XE, with 0^0 and 90^0 fibre direction. The ends have additional 2mm and 4mm thick XE $0^0/90^0$ at 150mm and 50mm from the supports respectively. This thickening of the webs is to better handle the concentrated shear forces at the support locations. The design went through several iterations in order to use the materials efficiently which resulted in the carbon fibre only being used in the flanges for stiffness, since it has a higher cost. A more detailed production drawing is provided in Appendix C.

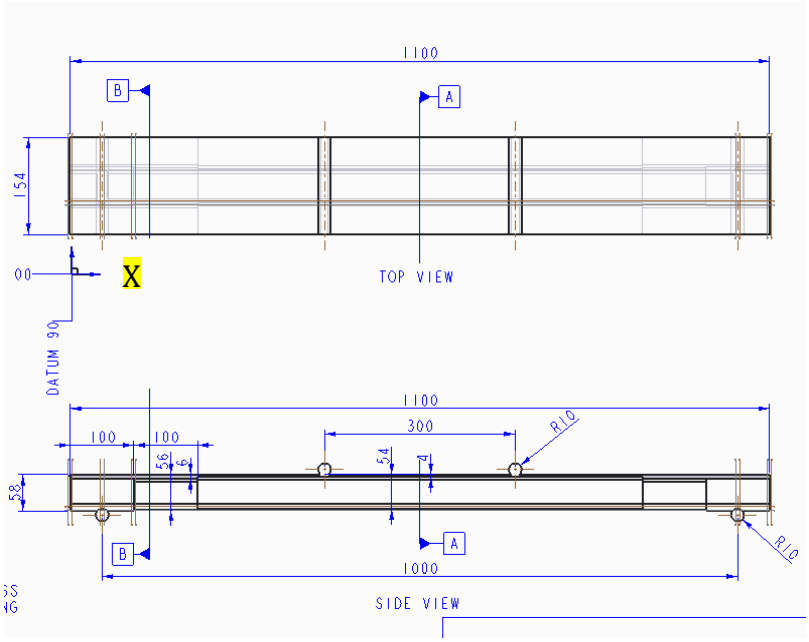

Figure 3-12: Hybrid Beam Production Drawing

A cost comparison was made between this CFRP/GFRP hybrid beam and an equivalent GFRP beam of matching mechanical properties, since there is a perception that using CFRP is not competitive on price. For equivalent flexural properties in the beam, the 1mm UC flanges could be replaced with 2.5mm XE flanges without changing the outer laminates. The CFRP flanges are found to be only 40% the thickness of the GFRP and this resulted in a weight reduction of the finished beam of approximately 23% for an increased material cost of 35% (Figure 3-13).

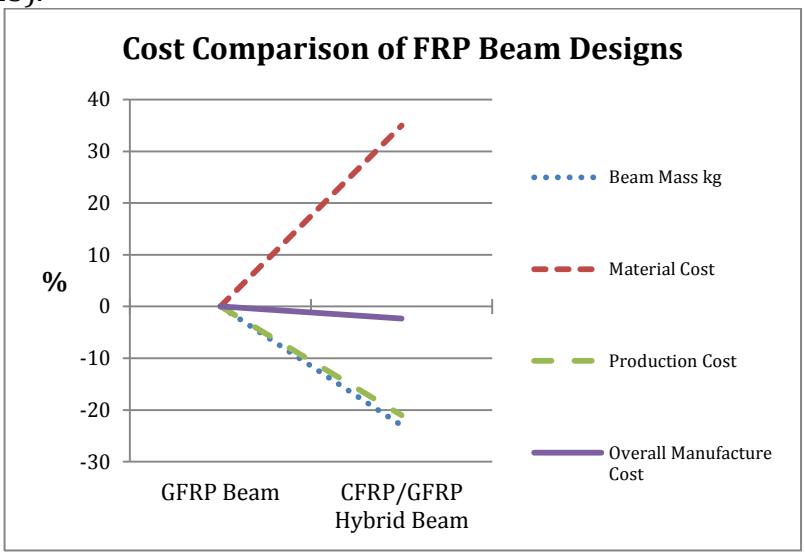

Figure 3-13: Comparison of GFRP Beam and Hybrid CFRP/GFRP Beam

Production labour costs would be slightly reduced since the number of overall layers to be processed has reduced (down by 17%), along with the time saved by the reduction in VE polymer required (down by 23%). For manufacturing in a developed country setting, where the materials to labour cost ratio is around 1.0, the reduction in production cost was estimated to be 20%. The conclusion was that the overall manufacturing cost of the hybrid beam would

be slightly reduced or close to that of the GFRP beam. Other than the weight reduction, the other net effect is the reduction in embodied energy with less materials and labour consumed. What is not considered is the additional engineering hours due to the complexity of the design, which is not significant.

The material properties used for the beam design were determined by mechanical testing of samples produced by vacuum infusion. The samples were each made six layers of reinforcement of biaxial E-glass 0/90 (600gsm) and unidirectional Carbon (330gsm) and low viscosity epoxy vinyl ester SPV6037 at 90kPa. A release fabric (peel ply) was placed below and above the laminate stack to aid in removal and to separate the infusion medium from the laminates for a more consistent surface finish. The setup is identical to the one shown previously in Figure 3-4. The results of the testing, tabulated below, was then used to complete the beam design and conduct finite element analysis (FEA).

Table 3-1: Mechanical Properties of Vacuum Infused FRP

	S.G.	*E Modulus 0^0 (GPA)*	*ult. Tensile Strength 0^0 (MPa)*	*E Modulus 90^0 (Gpa)*	*ult. Tensile Strength 90^0 (MPa)*	*v*	*In plane Shear Modulus G_{12} (GPa)*	*ult. In-plane Shear Strength (MPa)*	*Fibre Volume Fraction Vf*
XE 0^0 /90^0 in VE	1.9	22	352	22	352	0.3	4	50	0.65
UC 0^0 in VE	1.6	90	1213	10	50	0.29	5	65	0.64
PU foam	0.035	0.004	0.3	0.004	0.3	0.32	0.003	0.15	-

The flexural properties of the hybrid beam were determined by summing the *EI* values about the centroid *y'*. The foam core was neglected in these calculations for its very low tensile modulus of 0.004GPa. This was determined to add less than 0.1% stiffness and so could be disregarded in the bending calculation. The *E* modulus of the unidirectional carbon (UC) in VE laminates and biaxial glass (XE) in VE laminates were 90 and 22GPa respectively. The *EI* of the section was determined by the sum of the products of the E modulus and second moment of area, *I*, about the centroid for each sub section (Table 3-2)

Table 3-2: Hybrid Beam EI Calculation

Section	**Qty**	***A* (mm^2)**	***y* from top (mm)**	***Ay* (mm^3)**	***I* (mm^4)**	***D* (mm)**	***Ad^2* (mm^4)**	***E* (N/mm^2)**	***EI* ($N.mm^2$)**
deck	1	308	1.0	308	102.67	17.54	94801	22000	1.63E+09
Upper glass flange	1	200	3	600	66.67	15.54	48323	22000	8.06E+08
C flange top	1	50	1.5	75	4.17	17.04	14525	90000	1.02E+09
C flange bottom	1	50	52.5	2625	4.17	-33.96	57650	90000	5.83E+09
Lower glass flange	1	108	53	5724	36.00	-34.46	128218	22000	3.16E+09
glass webs	2	100	29	5800	20833	-10.46	10932	22000	1.6E+09
		916		**15132**					**1.40E+10**

Centroid	*y' top*	16.5
	y' bottom	37.5

The beam *EI* value was predicted to be 1.40E+10 N.mm^2. This was then used

for design calculations, such as moment and deflection, as follows. To simplify the calculations, the beam was assumed to have a constant cross-section and constant *EI* for the length of the beam. Deflections and slope angles were assumed to be small and only in the elastic region to reduce the terms in the equations. A three point bending case was used to determine if the beam was meeting the flexural target. For a simply supported beam with a span of *L* and a point load, *F*, at mid span, the equation for deflection, δ, can be expressed by:

$$\delta = \frac{FL^3}{48EI} \qquad \textbf{Eq. (11)}$$

EI is the flexural rigidity, assumed to be constant for the entire length of the beam. Using equation 10, the maximum deflection was estimated for a 2kN point load and a 1metre span as 2.98mm -which is a deflection ratio of 1/336.

For a four point bend (FPB) test, a free body diagram was drawn along with a shear and moment diagram to better determine the resulting actions (Figure 3-14).

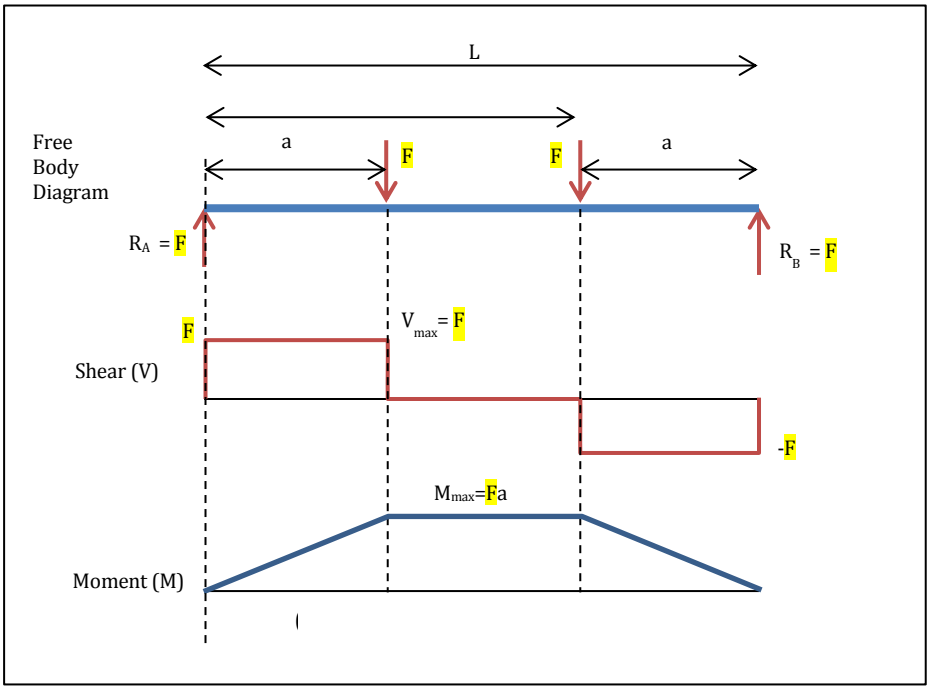

Figure 3-14: Free Body Diagram, Shear and Moment Diagrams for four point beam bending

For this four point bending problem we can derive expression s for shear, *V*, and moment, *M*, with respect to *x* length along the beam. For the region $(0 \leq x \leq a)$

$$V(x) = F \qquad \textbf{Eq. (12)}$$

$$M(x) = Fx \qquad \textbf{Eq. (13)}$$

And for the section $(a \leq x \leq b)$ the equations for shear and moment become:

$$V(x) = 0 \qquad \textbf{Eq. (14)}$$

$$M(x) = Fa \qquad \textbf{Eq. (15)}$$

For *F*=1000N and a=0.350m the maximum shear force is found to be *V*=1000N and the maximum moment is found to be *M*=350Nm. A maximum stress and strain was predicted in the lower flange made of biaxial glass to be 20.6MPa

and 934μm/m respectively. This is just under the 0.1% strain, above which micro-cracking may occur. So the beam is not expected to fatigue at loads below 2kN.

The deflection formula can be found as the sum of two off-centre load deflection curves by superposition.

$$\delta = \frac{\mathrm{Fb}}{6\mathrm{EI}}\left[\frac{L}{b}\langle x-a\rangle^3 - x^3 + (L^2-b^2)x\right] + \frac{\mathrm{Fa}}{6\mathrm{EI}}\left[\frac{L}{a}\langle x-b\rangle^3 - x^3 + (L^2-a^2)x\right] \quad \textbf{Eq. (16)}$$

A full derivation of the deflection formulas can be found in Tomishenko (1972). When a=350mm, b=650mm, L=1000mm, loads F=1000N and the mid span location is x=500mm, the mid-span deflection δ_{mid} is found to be 2.54mm, which is a deflection ratio of 394.

Shear deflection often needs to be considered since FRP beam designs often have thin webs. To test whether this has a significant effect on beam deflections and if it is considered a 'deep beam', a span/depth ratio < 5 is checked. With the span/depth ratio of the beam of 19.2 and considering the additional thickness in the webs at the end which reduce this effect, the shear deflection was determined to be negligible.

The maximum shear stress can be approximated by 1.5 times the average shear in the webs at the neutral axis - determined by Tomishenko and experimentally confirmed as being reasonably accurate by many others. This is represented by the following formula:

$$\tau_{max} = \frac{1.5\,V}{A_{web}} \quad \textbf{Eq. (17)}$$

τ_{max} is the maximum shear stress in the beam, V is the shear load, A_{web} the shear web area. Due to the fact that the flanges are relatively small in the vertical dimension, their contribution was neglected. So the area considered is only the web area, in this case is 200mm^2. The maximum shear force, when the two loads F=1kN, is V=1kN acting between the support and the load position. Using equation 17, we find the maximum shear stress is τ_{max}=7.5MPa. For a 1kN shear force the max shear strain, γ, was found to be 1500μm/m. In the webs closest to the supports, where the webs are thickened by a factor of 2 (150mm from the support) and a factor of 3 (50mm from the support), the maximum shear is predicted at 3.75MPa and 2.5MPa respectively. Failure is not expected in this region. Using these calculations, predicted stresses, strains and deflections are summarised in the following table.

Table 3-3: Hybrid Beam Design Calculations

Load (N)	*Max shear in web (MPa)*	*Max shear strain in web*	*Max deflection (mm)*	*Max strain in flange*	*Combined Strain in web*	*Stress in XE-0/90 web (MPa)*	*Stress in XE-0/90 flange (MPa)*	*Stress in UC-0 flange (MPa)*	*Deflection ratio L/d*
0	0.0	0.00E+00	0.00	0.000E+00	0.000E+00	0	0	0	
500	1.9	3.75E-04	0.64	2.335E-04	3.903E-04	9	5	21	1563
1000	3.8	7.50E-04	1.27	4.670E-04	7.805E-04	19	10	42	787
2000	7.5	1.50E-03	2.54	9.339E-04	1.561E-03	38	21	84	394
4000	15.0	3.00E-03	5.08	1.868E-03	3.122E-03	76	41	168	197
8000	30.0	6.00E-03	10.2	3.736E-03	6.244E-03	152	82	336	98
16000	37.5	7.50E-03	12.7	4.670E-03	7.805E-03	189	103	420	79
14000	52.5	1.05E-02	17.8	6.537E-03	1.093E-02	265	144	588	56
18000	67.5	22.9	25.56	8.405E-03	1.405E-02	341	185	756	39

Linear elastic behaviour was assumed for simplicity. The first mode of failure predicted is shear failure when the total load is in excess of 18kN for a 1.5% (15000με) maximum strain criteria located in the webs between the support and load locations. Failure in bending is not expected until loads exceed 36kN. In the case where deflection limits are set by design standards - span/250 in buildings or span/600 in bridges - a serviceability limit state for this beam would be range from 2 to 1kN respectively. The beam is representative of a full scale bridge beam or structural member that can be produced with embedded sensors and so will be tested at the 2kN service load to demonstrate its behaviour in this application range. In commercial full scale production, the geometry can be varied to have increased flexural stiffness and load capacity for optimising to specific applications.

3.14. Finite Element Analysis of Hybrid Beam

Finite element analysis (FEA) of a 2kN static four point bend at 1000mm span and 300mm load spacing was simulated to determine areas of stress concentration and potential sensor placement. A comparison of two software packages and previous hand calculations is made. This comparison is made to highlight the special treatment fibre composites require when conducting analysis and the likely error when using traditional 3D elements for a simulation.

A 2D element simulation was conducted in Strand7 using 2112-4 node 2D elements using individual ply mechanical properties. The maximum strains are predicted in the webs between the load point and the additional shear laminates of 991με. The bearing area at the supports also have high strains and the soffit of the beam has 750με. Mid span deflection was predicted as 2.21mm.

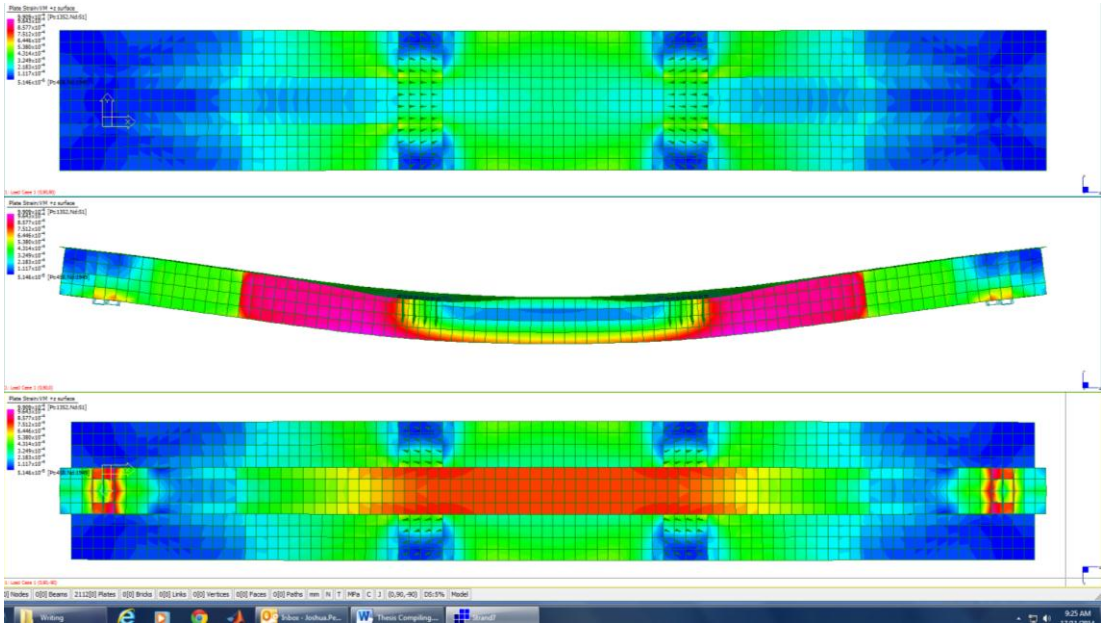

Figure 3-15: Strain Distribution of Beam under FPB -4 node 2D elements (Strand7)

Another simulation in Strand 7 utilised 20,492-8 node 3D elements to yield strain distributions in the following figure.

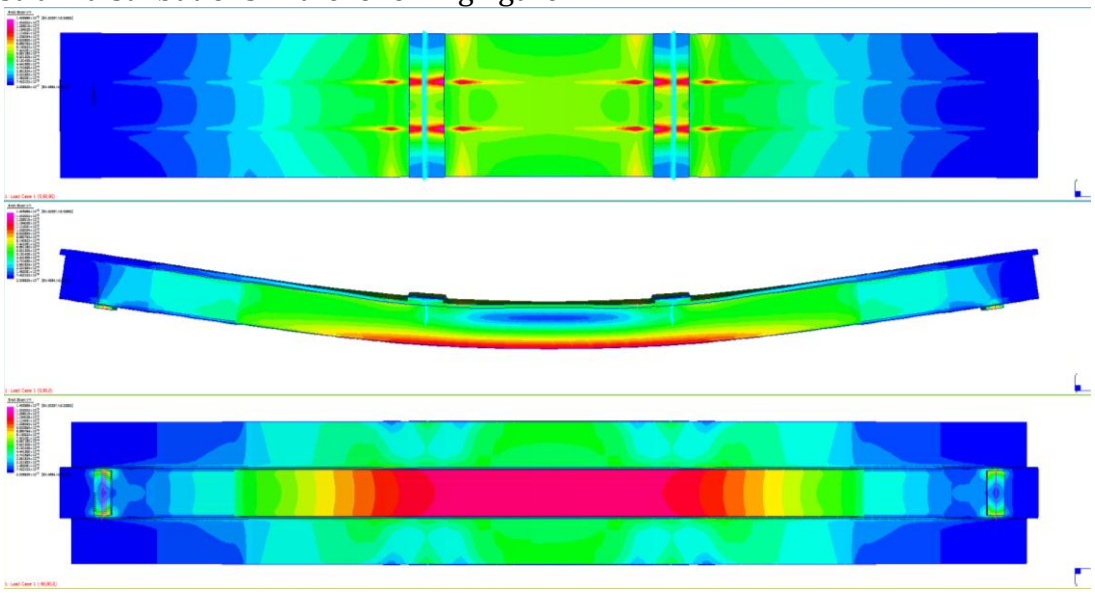

Figure 3-16 Strain Distribution of Beam under FPB -8 node 3D elements (Strand7)

The material properties were assigned as averages for each 3D block. High strains in excess of 1000με were predicted by the simulation at load points on the top surface and slightly less at the supports but the highest strains were found at the soffit of the beam with a value of 1406 με. The predicted maximum deflection was 3.01mm.

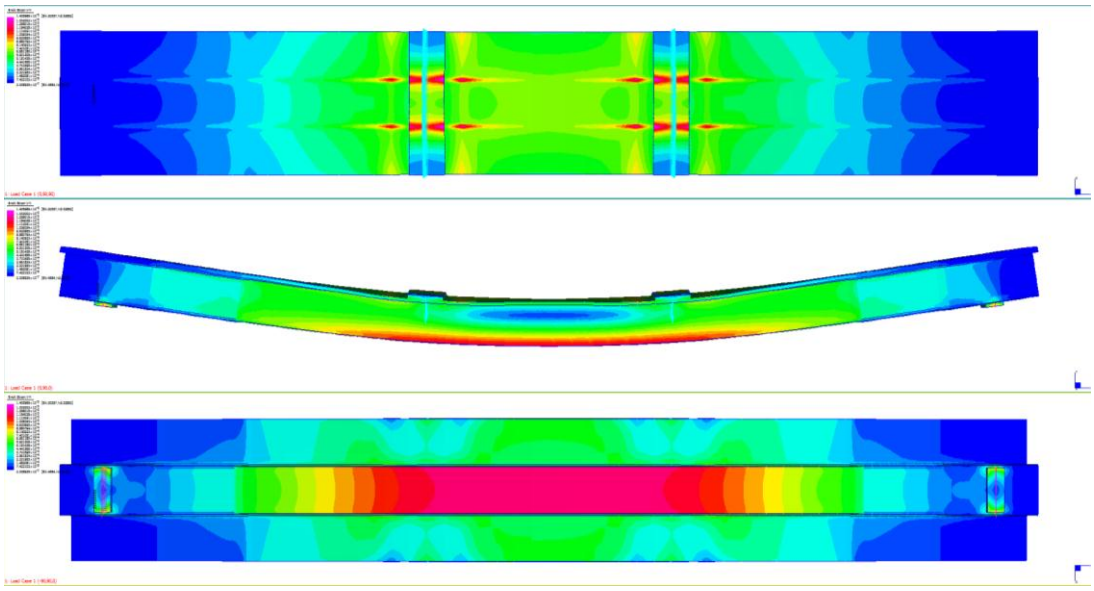

Figure 3-16: Strain Distribution of Beam under FPB -8 node 3D elements (Creo 2.0)

Simulation was also conducted in Creo Parametric 2.0 using 8node 3D elements to yeild maximum von-mises stress at the soffit of the beam of 29.5MPa, at the same location a maximum strain of 1344 με and a maximum vertical displacement of 2.21mm. The related figures are located in Appendix D.

A summary of the predicted strain and deflection values are detailed in the following table.

Table 3-4: Comparison of Deflection and Strain Predictions for FPB

	Estimate by Hand Calculations	Strand 7 4node Plate Element Simulation	Strand 7 8node Solid Element Simulation	Creo 2.0 8node Solid Element Simulation	Mean Value	Coefficent of Variation (standard deviation/mean)
Max deflection (mm)	2.54	2.21	3.01	2.37	2.53	0.14
Max Shear Strain in Web (με) [MPa]	1500 [7.5]	916	1103	626	1036	0.35
Max Tensile Strain in Lower Flange (με), [MPa]	934 [20.5]	774	1206	656	893	0.27
Max strain in beam	1722	991	1214	808	1184	0.33

The hand calculations used a conservative approach, but were the quickest to obtain a result. The geometry was simplified into rectangular sections so the fillets and rounds were not considered. The extra end shear laminates were not considered in the deflection calculation or in the shear strain calculation, so it can be seen that all values determined this way were at the high end of the range. The Strand 7 simulation using 8 node solid elements was the most innacurate. It considered the FRP as a solid isotropic material and not as orthotropic lamina. From the results it shows a higher mid span deflection than the hand calculations and is clearly an incorrect method for analysing FRP. Both the Strand 7 and Creo 2.0 simulations are believed to be the more accurate, since they calculated using

orthotropic material properties and the geometry was modelled with greater detail. The hand calculations predict the first failure mode to be in shear, whereas the finite element methods predict failure in bending. These failure loads only being 15% different to each other due to the optimisation in the beam design.

3.15. Manufacture of Beam with Embedded Sensors

The beam was fabricated upside down on a rigid glass mould surface. The following table details the order of layers for production.

Table 3-5: Layer Sequence for Composite Beam Infusion

Layer	Description
1	Glass mould surface waxed and polished area 1300x300mm for finished part 1200x200mm.
2	Peel ply -1200x200
3	8 layers 600gsm E-glass 00-90 full length-1200x200mm
4	4 layers 330gsm Carbon 00 full length for beam upper flange -1200x50mm
5	Cotton wadding as infusion medium under beam -1200x50mm wide
6	Foam core with channel milled for sensors path -1200x50x50mm
7	4 layers 330gsm Carbon 00 full length for beam lower flange -1200x50
8	Sensors threaded at mid span –channel filled with silicon rubber and fully cured
9	4 layers 600gsm E-glass 00-90 at 200 from end -200x300
10	4 layers 600gsm E-glass 00-90 at 100 from end -100x150
11	8 layers 600gsm E-glass 00-90 full length-1200x300
12	Peel ply -1200x300
13	Infusion mesh -1200x300mm
14	5 Infusion channels 300x50mm running perpendicular at 300mm spacing
15	3 ports –1 centre and 1 each end
16	Vacuum bag 1300x400 fixed with tacky tape 6m
	De-gas from 0-90kPa, Vacuum infuse at 80kPa, then raise to 100kPa to cure
	Trim to 1100x160 with diamond blade and sand surface with 120grit
17	Apply 1 layer 450gsm E-glass Chopped Strand Mat hand laminated over both sides full length as sacrificial surface layer

Since there is high stress in the soffit of the beam and the carbon and glass have differing elastic moduli, there is a possibility that the differing materials could delaminate because of fatigue or overloading. It was determined that a sensor in this location could monitor any delamination as well as normal bending in the beam. Note the fibre optic cable was recessed in the foam core and threaded through the carbon layers for the sensor position at mid span (Figure 3-17). The result is the sensor is between the carbon flange and glass outer layers.

Figure 3-17: Beam Manufacture: a) Fibre optic cable recessed in core, b) Carbon and glass layers

In Figure 3-17a it has been highlighted at the location where a small silicon delamination patch was placed covering half the length of sensor 2. This was made from a piece of silicon bagging material that resists resin bonding. It is anticipated that the readings of sensor 1 and 2 will show differences as the sensor is not fully bonded. This is to determine the sensor response to a delamination or due to improper embedding methods.

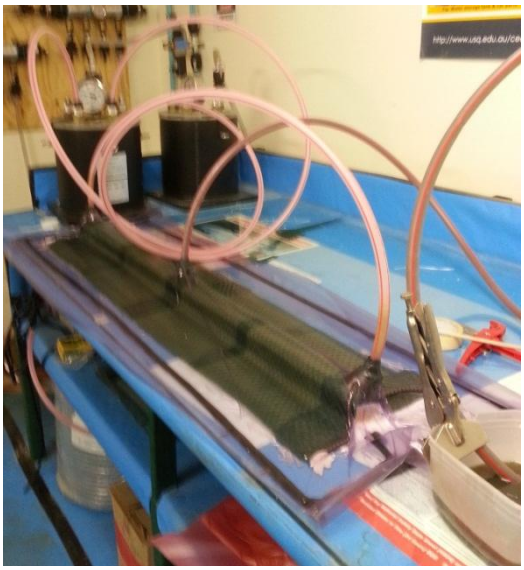

Figure 3-18: FRP Beam Manufacture by Vacuum Infusion

The vacuum infusion was setup with one centre inlet and an outlet at each end of the beam. Five low pressure channels were evenly spaced at 300mm and at inlet outlet locations to create an even resin front during the infusion process (Figure 3-18). MEKP catalyst of 1.8%wt was used and infused under 80kPa, then incraesed and held at 90kPa while curing. After curing and removing peel ply, a layer of chopped strand mat (CSM) was hand laminated over the entire surface as a sealing layer. This was followed by a brushed-on coating of resin mixed with a

surfacing agent (vinyl ester resin mixed with 2% wax in styrene), to simulate a finished resin coat or flow-coat typically applied on products.

3.16. Cyclic Testing of Beam

Cyclic testing was performed on an MTS machine with a 100kN capacity (Figure 3-19). Steel load beams were prepared to load at 300mm spacing and 1000mm span. Steel plates, 5mm thick, were placed at load points and at the supports to reduce effects due to concentrated loads.

Figure 3-19: Cyclic Testing on MTS 100kN Hydraulic Cyclic Testing Machine

The test was carried out in batches of 10,000 cycles at 2.5Hz in a load range of 0.5 to 2.0kN to represent the scaled beam under service loads (Figure 3-20). After 100,000 cycles with little to no change, the loads were progressively increased to 3, 4 and 5kN until completing testing after 250,000 cycles. This was done to introduce overloading to cause fatigue and to test the sensor response. Between each batch of 10,000 cycles, FBG readings were taken during a static test at no load and at 2kN. The readings of peak data and full spectrum data were compared to determine any evidence of damage to the beam. This is to simulate the inspection and test of an actual beam in situ. A non-destructive load, in the range of a service load, is applied while readings are taken and then compared over time. For the FBG smart beam system to be successful, the sensors need to demonstrate reliability over repeated use and to accurately detect a decline in performance of the beam.

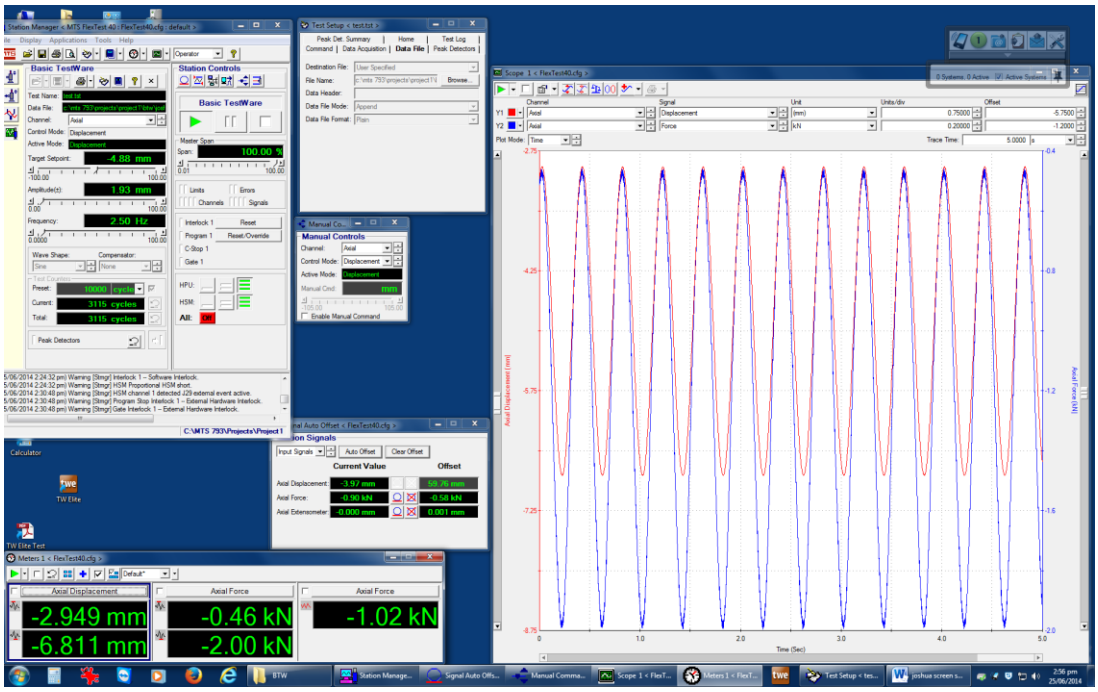

Figure 3-20: Cyclic Loading Displacement Control

The control system was set for displacement targets corresponding to the 0.5 to 2.0kN loads. At the start of each batch, the displacement targets would have to be reset. This was chosen because the test machine can accurately position itself at higher cycle speeds than if it was set to load target control.

3.17. Summary

Optical sensor embedding techniques were addressed to improve the manufacturability of smart composite structures. These embedding methods were improved and the results are discussed.

Fibre optic sensors where embedded in a scale model GFRP bridge deck panel during manufacture. The panel was tested under various uniformly distributed loads. Sensor data was collected and a strain signature was developed for each load case. A Finite Element Analysis was used to predict strain data at sensor locations and these were found to correlate well with the experimental values. Software was used to inversely predict distributed loading from the strain data with good accuracy.

Damage, to simulate small cracks, was also introduced to the panels by machining and these were tested for increases in strain and distortions in the reflected spectrum. Several indicators where used to describe these distortions: full width at half maximum (FWHM), distortion index and a novel gradient of symmetry.

A hybrid CFRP and GFRP model beam was designed and manufactured with embedded FBG sensors. This beam was tested under cyclic loading to determine the long term behaviour of the sensors and their ability to detect early signs of fatigue.

It was found that both the distortion index and the gradient of symmetry were superior at detecting damage near to the sensor location than the FWHM. The gradient of symmetry was found to be more sensitive to changes in the spectrum than the distortion index. Finally, it was found that using these

indicators together with strain values was more reliable at detecting damage early.

4. DATA ANALYSIS

An optical data acquisition system was set up (

Figure 4-1) with an optical interrogator connected to the FRP structure by an optic fibre cable and to a PC with analysis software and post processing software. The optical interrogator, Micronoptics SM125, provided a tuneable laser light source and a tuneable filter measuring 4 channels at 1Hz with an accuracy of +/-10 x10^{-12}metres (+/-10 picometres).

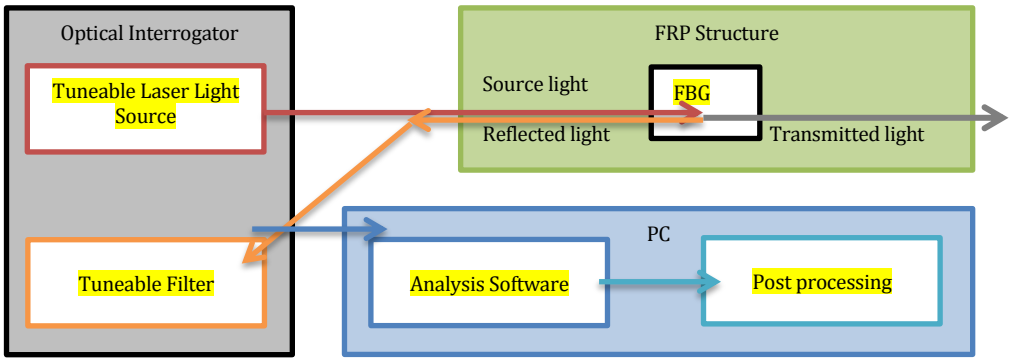

Figure 4-1: Data Acquisition for FBG Optical

The analysis software was able to provide data in the form of spectrum peak wavelengths and full spectrum data. The peak wavelengths are determined in an unknown way by the software and exported as a data file. The full spectrum data collected was in the form of a data file with 16000 coordinate points of reflected spectrums (in decibels) over a wavelength range for each load. A simple post-processing program was developed using Matlab to read these data files, simplify the data analysis and plot the key information for interpretation by the operator.

The reflected spectrum showed distinct peaks with a fairly consistent shape throughout the loading (Figure 3-9). The top of the peaks showed some noise that was treated by applying a seven point average function to smooth the data. Minor peaks indicated distortions existing in the sensor due to sensor manufacture and possibly uneven curing rates in the FRP.

4.1. Strain

The peak data collected was in the form of peak wavelengths in a comma separated variable file (.csv) and was converted to strain values by equation 10 presented earlier. Initial residual strains were found in the material caused by shrinking during polymer curing. Further strain values where calculated with this being the reference value. These residual strains were approximately -170x10^{-6} strain which corresponds to a residual stress of 3.7MPa in compression (E=22GPa).

4.2. Normalising Power Range

Due to possible fluctuations in the power transmitted through equipment which in turn causes fluctuations in the power (dB) reflected, it was important to normalise the power range for clear comparison. The spectrum was normalised to values between 0 and 1 by subtracting the minimum power and dividing by the power range for each sensor, which can be described by equation 18:

$$P_{i\_normalised} = \frac{P_i - P_{min}}{P_{max} - P_{min}} \qquad \text{Eq. (18)}$$

This will ensure further comparisons of the spectrums are valid.

4.3. Peak Detection

When the reflected spectrum shows distortions or a chirped pattern, there can be difficulty in detecting the peak wavelength. Peak detection was trialled using the 95% of maximum data points since little distortion is found below this level. A midpoint wavelength is found between the two points as an estimated peak wavelength, as shown in Figure 4-2.

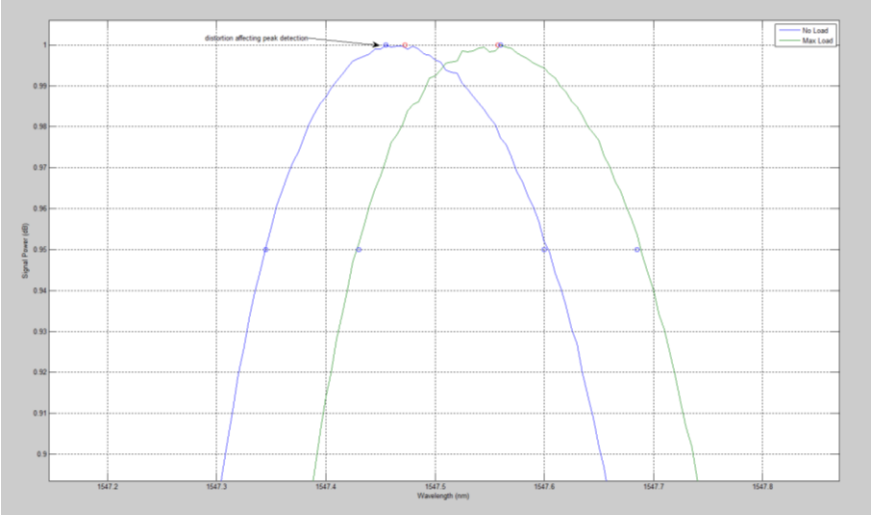

Figure 4-2: Peak Detection using mid-point wavelength of 95% of maximum power

At times this was found to be almost identical to the peak data recorded but where chirping occurred, as in the signal on the left, the estimated peak showed some difference. The outcome of using this estimate as opposed to the recorded peak showed promise and will be discussed further in the results chapter.

4.4. Spectrum Indicators

To aid in tracking the peaks and spectrum distortions, indicator points where chosen at 95%, 70% and 50% of maximum power (Figure 4-3). The reason for choosing these is detailed as follows. The spectrum width at 50% is also known as full width at half maximum (FWHM) and is commonly used in signal analysis. The 95% indicators tend to fall below any chirping near the peak of the spectrum while being able to describe the width near the top. The 70% indicators are roughly halfway between the 50% and the 95% indicators to describe the continuity of the shape.

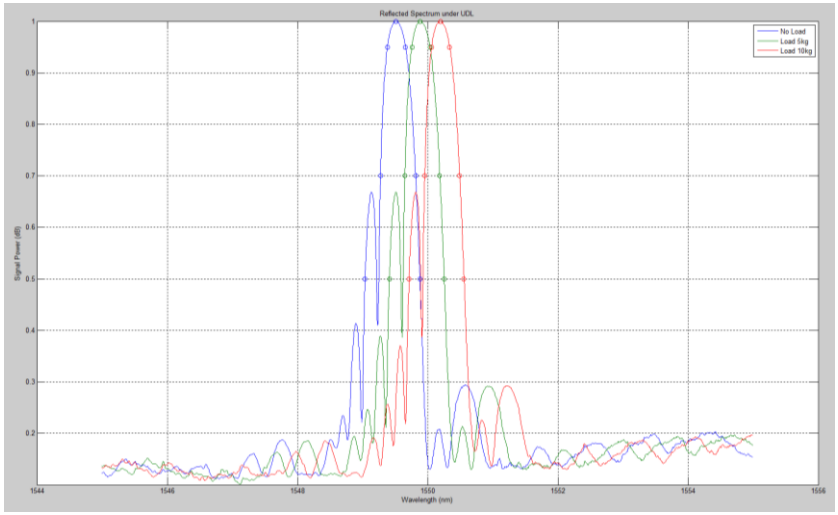

Figure 4-3: Normalised Spectrum with Spectrum Indicators when loaded at 0, 5 and 10kg.

The spectrum indicators are proposed to be a simplified method for tracking changes in the spectrum and to aid in peak detection without handling large amounts data. Finding ways to better track the spectrum is believed to deliver better SHM using FBG's.

4.5. Spectrum Shape Factor and FWHM

One approach to compare the reflected spectrum over time is to take the full width at half maximum (FWHM) and divide by the power range to give a type of shape factor. This distortion index was trialled by Kahandawa (2012) to indicate damage. Changes in this factor over time are then tracked for large changes. Little change in the plot of FWHM indicates clear peaks are present in the spectrum and the width of the spectrum shape is not changing. The width of the 50% indicators after normalising the power results in the identical calculation.

4.6. Gradient of Line of Symmetry

The new approach proposed in this these is to indicate the level of distortion by the gradient of the line of symmetry of the spectrum. The concept is to measure the difference from the recorded spectrum to an ideal spectrum shape. An ideal spectrum has an axis of symmetry that is vertical -that passes through the peak and the midpoint of the width at any height (Figure 4-4).

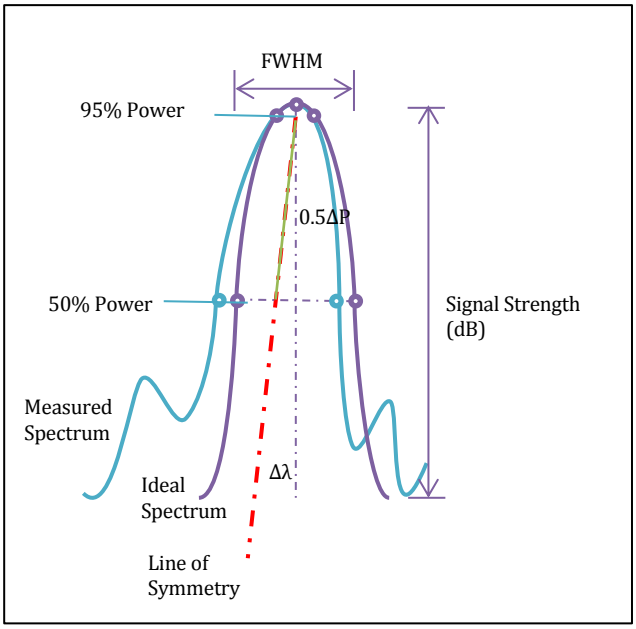

Figure 4-4: Gradient of Line of Symmetry

To determine the variation from ideal spectrum, the gradient of the line passing through the mid points of the widths at 95% of maximum and 50% of maximum power is found. Both the sign and magnitude of the gradient indicate the shape of the spectrum.

$$G = \frac{0.5\Delta P}{\Delta\lambda_{mid}} = \frac{P_{95}-P_{50}}{\lambda_{mid95}-\lambda_{mid50}} \qquad \textbf{Eq. (19)}$$

The power at 95% and 50% of maximum are found, P_{95} and P_{50} respectively, then the middle of the centre wavelength is found for both power levels, λ_{mid95} and λ_{mid50}. The linear gradient of this line is then tracked over successive loading cycles to track changes in the spectrum shape and is proposed to be more descriptive of the spectrum than FWHM as it has both sign and magnitude. A positive gradient indicates that a greater area is found at a lower wavelength than the peak (Figure 4-4) and a negative gradient indicates that a greater area is found at a higher wavelength than the peak. Dramatic changes in this gradient is proposed to indicate evidence of combined loading and possibly early failure detection.

4.7. Summary

The data acquisition system was described with the method of collecting peak data and full optical spectrum data. The steps of normalising the power range and detecting peaks was explained. Some novel spectrum indicators were presented and how they are calculated in order to describe the spectrum over time and monitor changes to it. These indicators were used to track changes in the spectrum of FRP structures under load and with introduced damage.

5. RESULTS AND DISCUSSION

The results presented cover the load testing of the smart FRP deck and the FBG sensor response. Next the cyclical loading response of the smart FRP beam is detailed along with the spectrum indicators change with fatigue and overloading.

5.1. Deck Test Results

5.1.1. Simply Supported UDL

The deck with sensors in locations presented in Figure 3-5 was tested as a simply supported on two sides deck with a UDL. The following figure shows data collected for the two sensors at 0^0 to axial direction of bending (00-1 and 00-2). These have the highest strains recorded as they are in the direction of bending. The strain values from the spectrum peak, the 95% mid wavelength and the FEA prediction were compared.

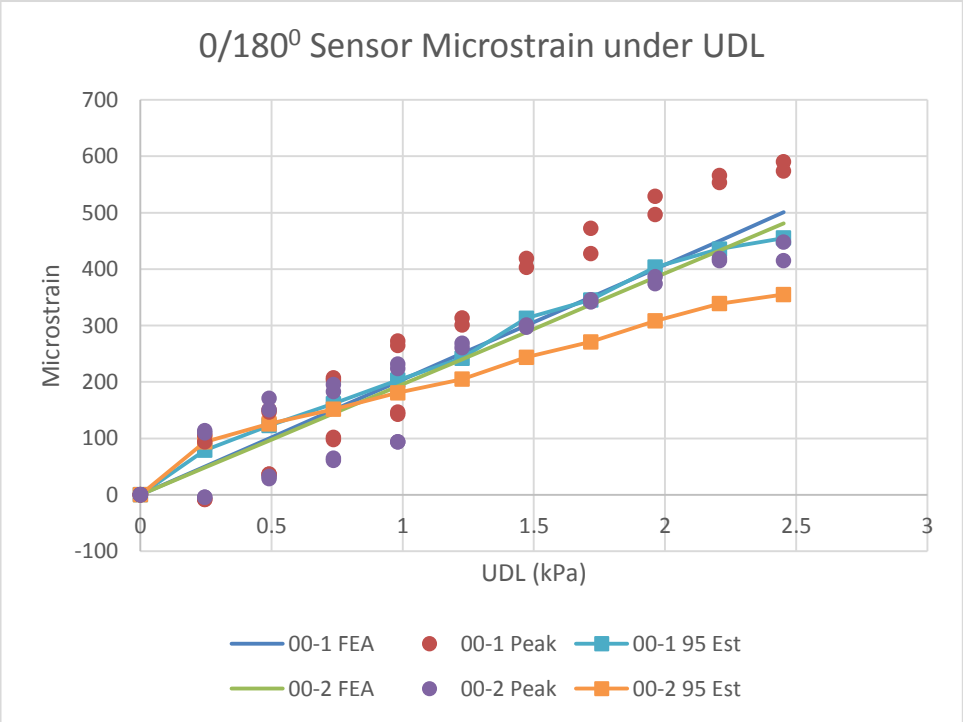

Figure 5-1: Strain from Sensor Data for Uniformly Distributed Load

It is clear that the estimated strain calculated from the 95% indicators have better accuracy in strain prediction than the peak data when compared to the FEA predicted strains for these tests. The standard error or mean squared error (MSE) was calculated, as in equation 14, for all sensor data.

$$MSE = \frac{1}{n}\sum_1^n(\mathbf{Y}' - \mathbf{Y})^2 \qquad \textbf{Eq. (20)}$$

Where, $\mathbf{Y}'$=vector of predicted values from FEA; $\mathbf{Y}$=vector of actual values (load test); n=number of samples. The square of the difference between predicted and measured strain values is then averaged for all loads for each particular sensor. This then gives a mean squared error for a particular sensor. The results are detailed in Table 5-1.

Table 5-1: Mean Squared Error of Microstrain Compared to FEA Prediction

Sensor	Mean Squared Error of Peak Data	Mean Squared Error of 95% indicator
00-1	87	19
00-2	61	38
45-1	42	39
45-2	36	33
90-1	13	10
90-2	22	11

It is clear that for all sensors the mean squared error was less for the calculated peak from the 95% indicators than from the actual data spectrum peak. The largest improvement in accuracy was found from the sensors under the largest tensile strain –sensors 00-1 and 00-2. This shows that this peak detection procedure, using the 95% indicators, can result in better strain readings than traditional peak data for this load case.

5.1.2. Distortion Indexes

The spectrum tracking, in the form of the FWHM and the novel gradient of symmetry of the spectrum, were derived from the full spectrum data and presented in the following figures.

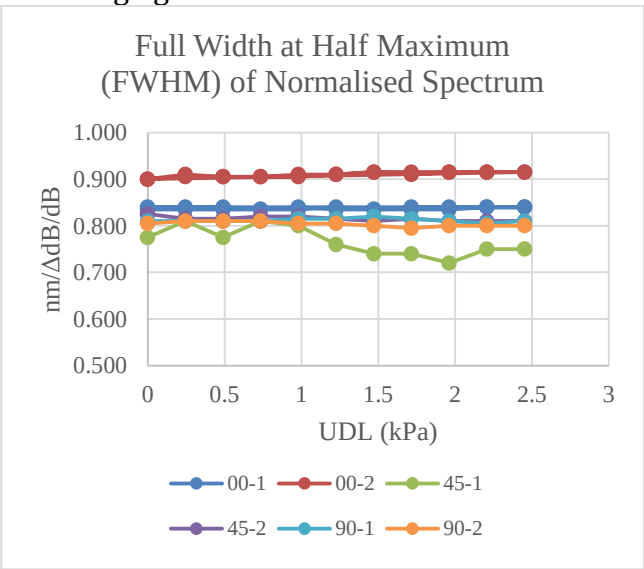

Figure 5-2: Changes in FWHM of Reflected Spectrum under UDL

The FWHM of the normalised spectrum was compared with its original no load value to determine the distortion index.

Little change in the plot of FWHM indicates clear peaks are present in the spectrum and the width of the spectrum shape is not changing. The sensor 45-1 does show a drop which indicates a narrower spectrum than expected. This change is around 10% and since it is not permanent for higher loads, indicates bending in the optic fibre and not damage to the FRP. This localised bending is

caused by the bidirectional fibre reinforcement in the FRP pressing on the optic fibre.

The gradient of symmetry of the spectrum was plotted for the simply supported decking panel with respect to the load (Figure 5-3). This gradient line was found by the 95% and 50% spectrum indicator points, as presented earlier.

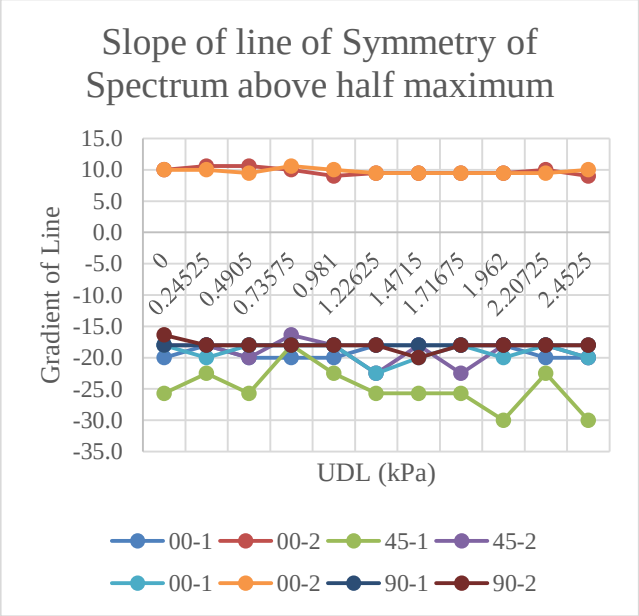

Figure 5-3: Changes in Gradient of Line of Symmetry of Spectrum

The gradient calculation appears fairly constant and stable for the 0 and 90 degree sensors but appears to be a little sensitive for the 45^0 sensors. This variation is consistent with the variation in FWHM for these same sensors. Generally, without major changes present, they indicate a good spectrum where a clear peak is present and the reliability of the reading is considered very high. The mechanism causing the change is the localised bending in the sensor within the GFRP. The 45^0 sensor operates between two XE 0/90 layers.

5.1.3. Damage Detection in Deck

The simply supported load tests were conducted as before (under UDL) but with a 1mm 'v' notch simulated damage incrementally increasing in length up to 20mm. The strain readings and distortion indexes where used to track the changes in the signal spectrum of all the sensors. The two that showed the largest changes were 00-3 (25mm from the damage edge in the x direction) and 90-1 (55mm from the damage edge in the y direction).

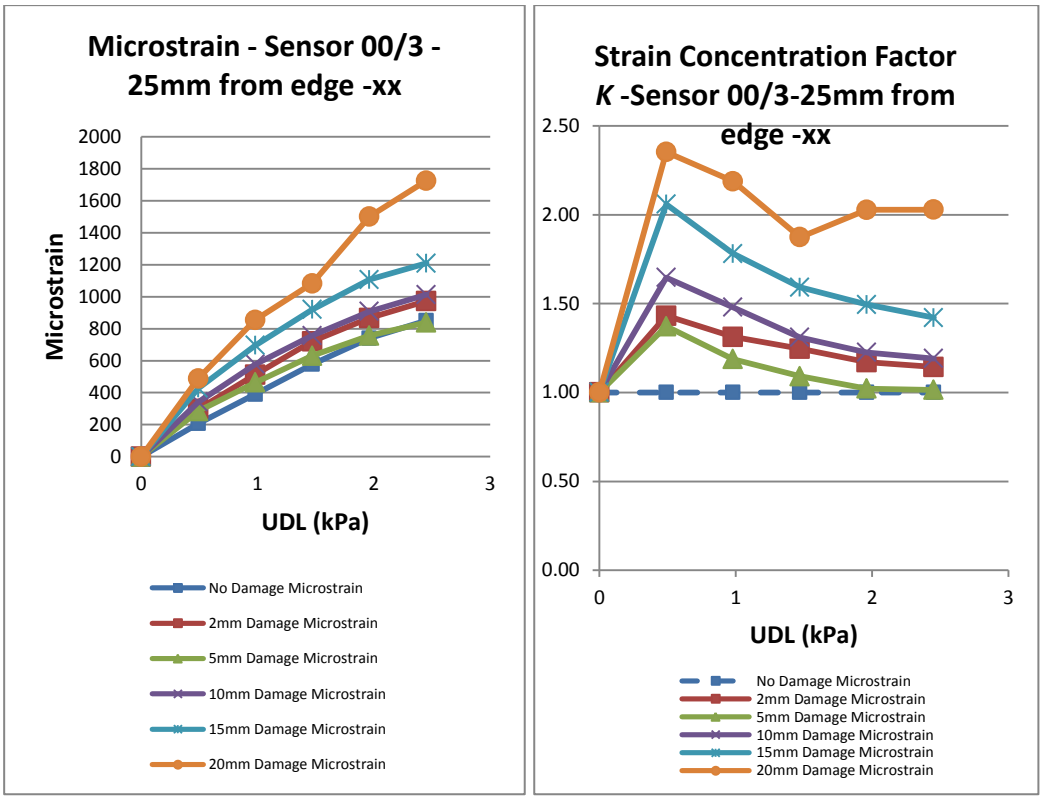

Figure 5-4: Strain Readings with increased Damage: a) Microstrain and b) Concentration Factor *K*

The strain concentration factor K ($K = {}^{\epsilon}/_{\epsilon_1}$) for the 0^0 sensor started at 1.4 for the smallest damage length (Figure 5-4b). This indicates that an FBG SHM system monitoring strain alone is capable of detecting excessive strain due to the damage.

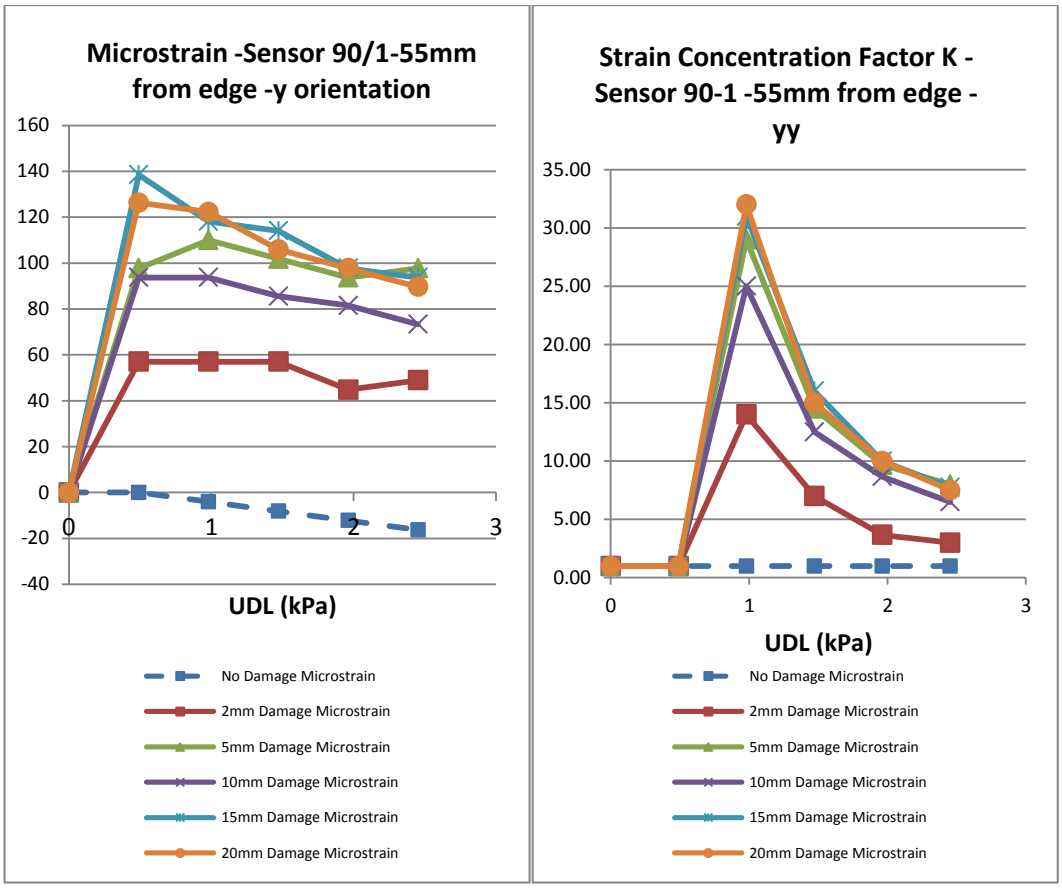

Figure 5-5: Strain Readings with Damage a) Strain, b) Strain Concentration Factor

The strain values for even the smallest size damage are significantly larger than those with no damage which indicate strongly that strain values parallel to the damage are be used a damage detection method.

The strain concentrations *K* for the 90^0 sensor where found to be quite high even for the lowest size damage recorded (Figure 5-5). For the 2mm size damage a *K* of 32 was found even though this sensor is 55mm away from the damage. The *K* factor reduced as the load increased due to the transverse bend towards the unsupported edge. At the highest load with a 2mm damage there was still a significant *K* value of 3.0. Since the undamaged panel had strains ranging between only 0 and -20με this sensor data is not very accurate and sensitive to uneven loading, which is seen in-situ.

The strain values and concentration factors are summarised in the plot for the largest load of 2.45kPa to better determine the trend (Figure 5-6).

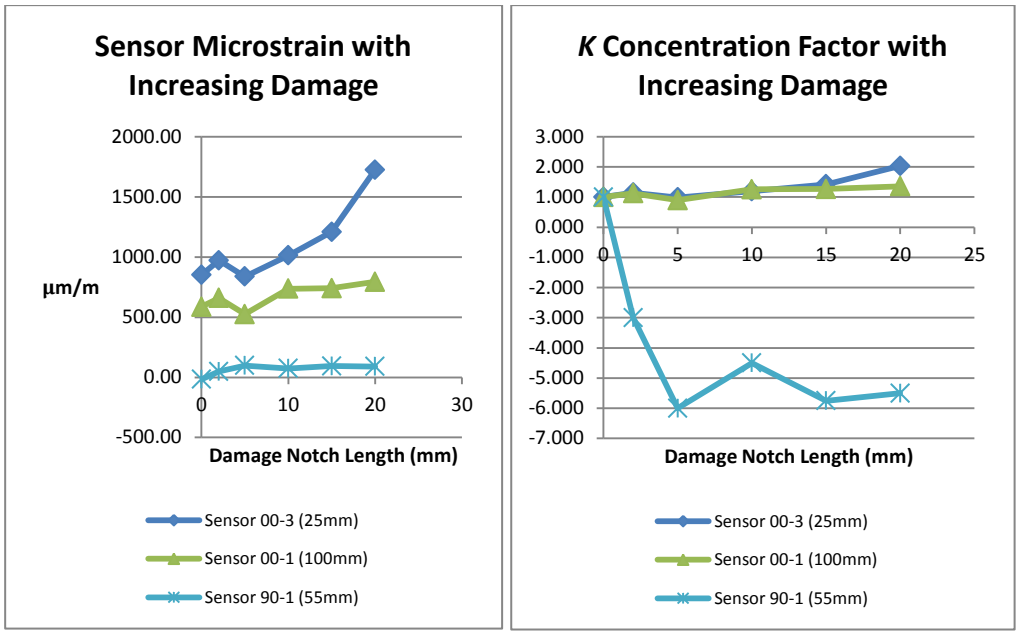

Figure 5-6: Effect of Increasing Damage on: a) Sensor Microstrain and b) *K* Concentration Factor

Increases in strain are present for all three sensors with the 90-1 showing the earliest change and largest *K* factor of 6.0. This was expected from the FEA prediction that the 90 degree strain showed a larger change. Both the 00-1 and 00-3 sensors show noticable increases in strain when the damage exceeds 5mm in length. These steadily increase as the damage increased to 20mm in length with *K* factors of 1.35 and 2.03 for these sensors respectively.

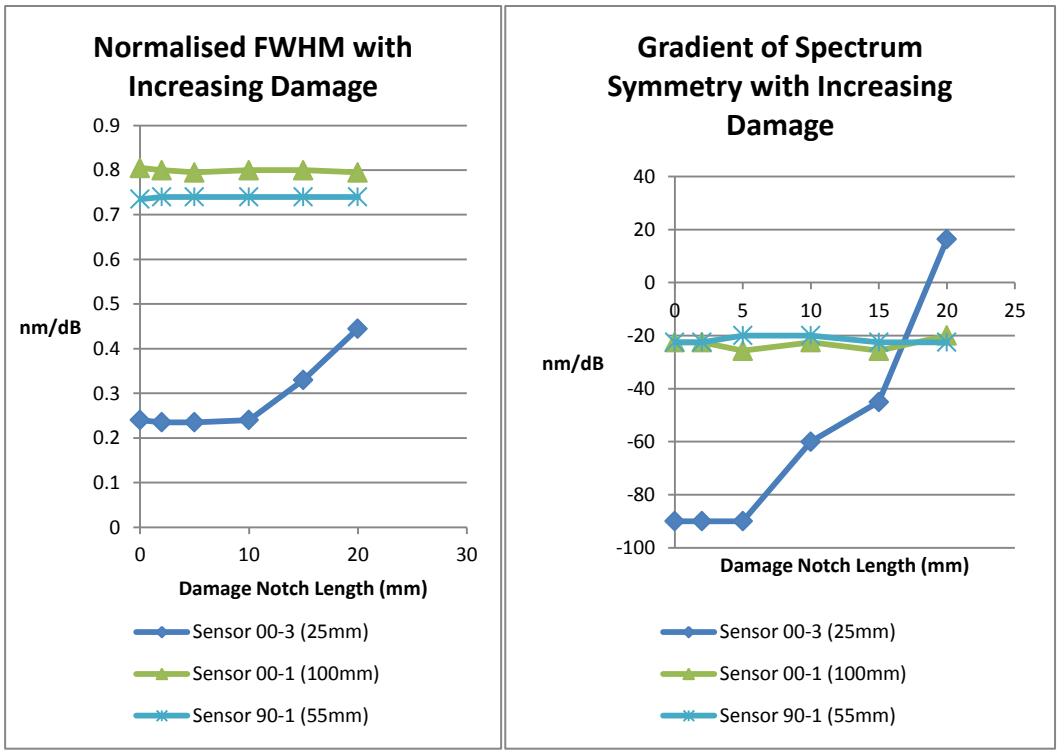

Figure 5-7: Effect of Increasing Damage on: a) Normalised FWHM and b) Spectrum Gradient of Symmetry

The changes in the normalised FWHM were not apparent until the damage

exceeded 10mm in length for the closest sensor 00-3 (Figure 5-7). As the damage was increased the FWHM plot shows a steady increase for this sensor. The other two sensors closest to the damage showed little change. This indicates that FWHM tracking alone is not very reliable in detecting small size damage. This data can aid in determining if damage exists when increased strains are present but not in isolation. Once the damage is larger than 10mm it may be detected by a visual inspection without the need for sensors. In large structures, this can be difficult, especially were access in restricted.

A similar indication is found from tracking the gradient of the line of symmetry: beyond the 5mm size damage, the gradient for sensor 00-3 is changing significantly. This is detecting the anomaly earlier than the FWHM method but not as early as the strain measurement.

For early damage detection using FBG sensors, it is proposed to map the following parameters: *K* concentration factor (ϵ/ϵ_1) and change ratio of the gradient of line of symmetry, *G/G1*. When both of these are indicating out of their normal range, a damage can be predicted.

5.2. Beam Results

The hybrid beam was tested in four point bending with a load of 2kN between batches of cyclical loading of 10,000 cycles. Further detail of the test set up is found in section 3.16. The embedded FBG responses were recordered for strain measurements and spectrum tracking.

5.2.1. FBG Response

The initial FBG response at no-load and at 2kN shows a clear peak for both mid-span sensors. As expected the optical response to the load applied is an increase in wavelength seen by the shift to the right direction of the page. Theses wavelength shifts correspond to a strain of 863×10^{-6} and 816×10^{-6} for the corresponding sensor locations 1 and 2.

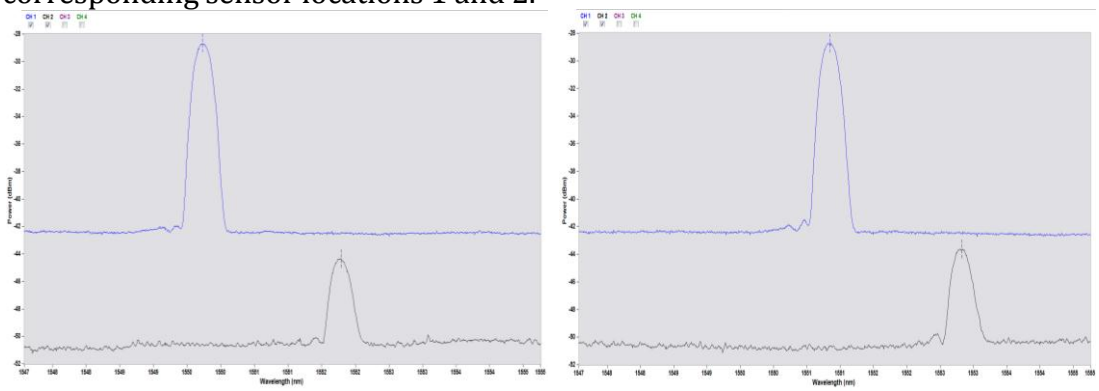

Figure 5-8: Embedded FBG Spectrum at: a) No Load and b) 2kN

The peak wavelengths were converted to strain values using equation 10 and plotted with respect to the cycles completed (Figure 5-9). The cyclic loading up to 1×10^5 cycles were conducted with the service of 2.0kN and show little increase in strains from the static tests. As the loads increased beyond 2.0kN, a rise in strains in the static test is evident.

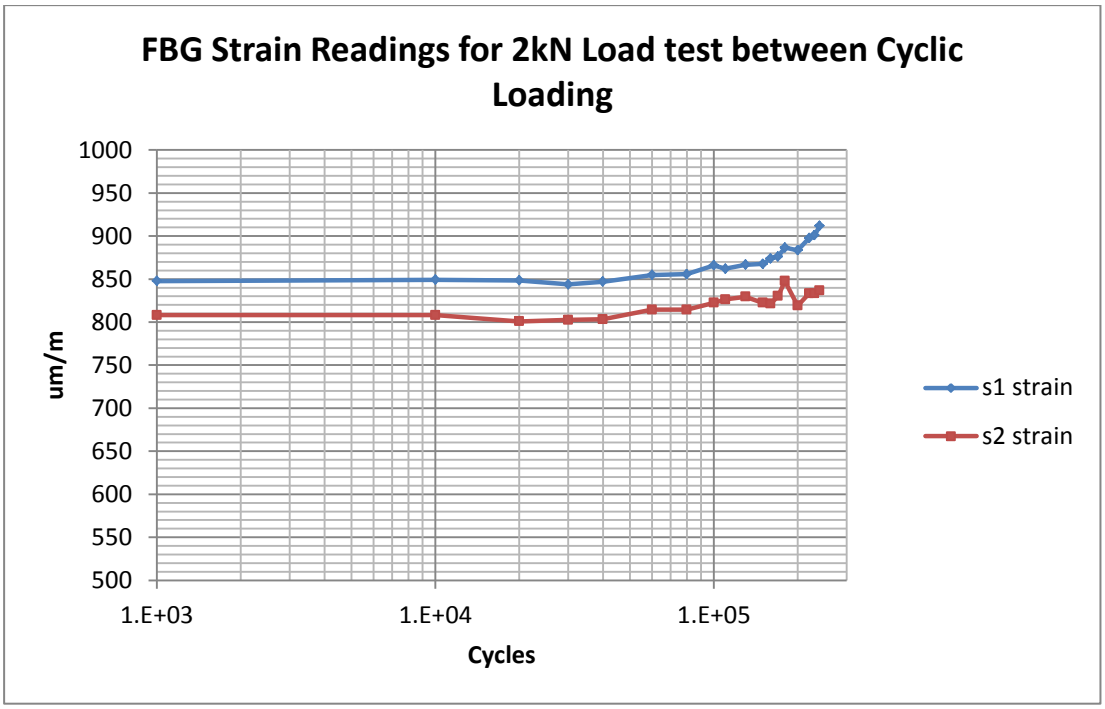

Figure 5-9: Strain Readings from static test between progressive cyclic loading

As the cyclic loads were increased to introduce fatigue, the static test strain readings increase gradually. It was observed that the mid span deflections also increased gradually. A difference in the increase in sensor 1 and sensor 2 readings was also observed. Sensor 2 had the silicon delamination patch covering half its length and this is believed to be causing slipping and more erratic readings. Sensor 2 started with a reading 95% of the sensor 1 but had a final reading only 91% of that of sensor 1. This can be an indication of the sensor de-bonding or of a delamination.

Figure 5-10: Early Signs of Fatigue in the Beams Outer CSM Layer

Early visual signs of damage were observed to the outer CSM layer on exterior of the webs (Figure 5-10). The appearance is lighter in colour as the layer has delaminated from the structural layers of the web. It resembles large blisters or bubbles. This layer is a sacrificial surface layer that is not part of the design calculations of the beam, but is common practice to seal and protect the structure. It can also aid as a visual cue of overloading or fatigue.

Strain readings taken after the increased load tests showed residual strain in the beam (Figure 5-11). Both sensors show a sharp increase at 10,000 cycles

when the cyclical load was increased to 3kN. This residual strain can be one sign of damage to the FRP structure.

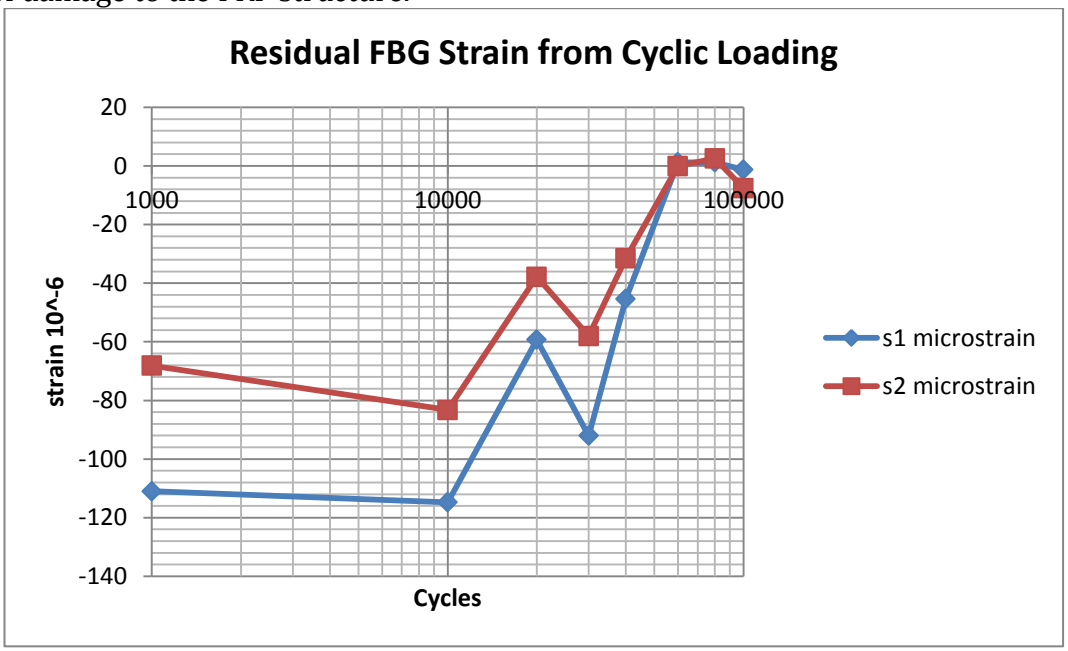

Figure 5-11: Residual FBG Strain from Cyclical Loading

A closer look at the increase in strain from the static tests can produce a linear approximation of the fatigue. The following figure uses a line of best fit to indicate the slope. The future state of the FRP beam, including remaining serviceable life can be predicted.

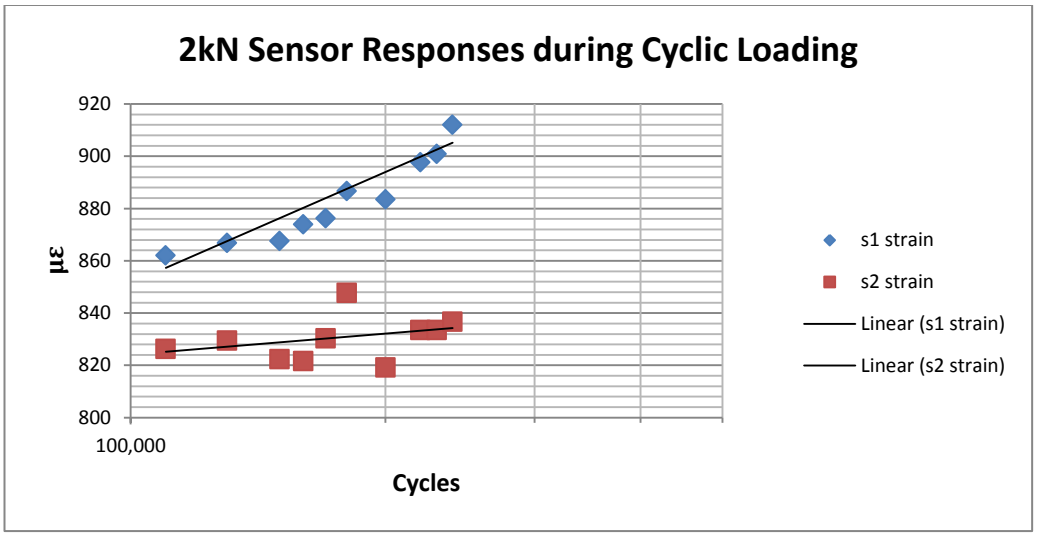

Figure 5-12: FBG Strain from 2kN FPB under Cyclical Loading

5.3. Summary

The results of the deck testing showed the ability for FBG sensors to be embedded in a prototype GFRP deck to measure strain. The sensors data successfully detected the simulated damage and it was found that using strain values alone could detect damage. The sensors in the network that were under the greatest tension were the most reliable at showing changes in the strain

reading. The spectrum data and indicators presented were used to track changes in the spectrum during loading. These showed significant changes during loading of the damaged deck.

The CFRP/GFRP hybrid beam was tested under four point bending with embedded FBG sensors and was found to measure strain accurately. Under cyclical loading, below the endurance limit of the material, the strain readings and spectrum data showed little change. When the cyclic load was increased above this threshold, the strain data showed increases and the spectrum indicators also showed increases. The progressive fatigue failure of the beam could be tracked using strain and the spectrum indicators.

6. SUMMARY AND CONCLUSION

6.1. Summary of Findings

Fibre optic sensor embedding techniques were refined for manufacturing FRP components. Locating the sensors was best done by threading a hooked needle followed by a small tube that the sensor is threaded into. The small tube is removed leaving the sensor in position. Using silicon rubber doping was found to be the most effective way of protecting the fibres at ingress/egress locations. These techniques were found to be the most reliable, accurate and quick.

FBG sensors were embedded into an FRP deck concept in order to produce a smart deck with in-built SHM capabilities. The deck was tested under UDL to a pedestrian type load level and the optical sensor data was collected. The optical spectrum was analysed by selecting indicator points at the maximum, 95%, 70% and 50% of maximum. The spectrum width was measured at these points and the middle wavelength was calculated in order to describe the spectrum mathematically. It was found that the middle wavelength at the 95% of maximum power was a more accurate value to calculate strains than the actual peak wavelengths recorded when compared with the FEA predictions.

Damage was introduced by a milling a small notch in the deck surface and the UDL tests were repeated. It was found that direct strain measurements were still the most reliable method for detecting damage under known loads. This combined with other spectrum indicators can give a better confidence in interpreting FBG spectrum data were full spectrum data is available. The FWHM method and the proposed gradient of the line of symmetry were compared for ability to indicate damage. It was found that gradient line method had a better range for predicting damage even at early stages. Where damage existed, both the stress/strain concentration factor K and the gradient line G indicated large changes from those without damage. It is envisaged that these in combination will increase the ability for early damage detection.

A CFRP/GFRP hybrid beam was produced with embedded FBG sensors. One sensor was ‘forced’ into de-bonding inside the beam. Under cyclical loading the sensors showed reliable measurements. When cyclical loads increased, the sensors showed residual strain under no-load and increased strain under the test load. The sensor with the de-bonding showed reductions in strain measurements compared to the other sensor.

6.2. Implications

This research has shown that FBG sensors are suitable for FRP structures for load detection, small damage detection and under cyclical loading.

The improved embedding techniques apply not only to FBG sensors but other fibre optics in the future. These same techniques can be extended to be used with resin transfer moulding, pre-impregnated fabrics and natural fibres.

It was shown that smart FRP structures can be designed and manufactured with embedded FBG sensors –specifically a bridge deck and a bridge beam.

6.3. Further research

Future research following from this can be in implementing the embedding

methods in to full-scale components, such as FRP bridge girders and FRP decking. These embedding methods may be trialled with other types of fibre reinforcement, such as aramid, basalt or natural fibres. Further investigation of the optical spectrum response is needed to establish a solid correlation between the spectrum shape and mechanics of the materials.

6.4. Conclusion

It is clear that FBG sensors are suited to structural health monitoring of fibre composites: specifically the engineering structural materials of CFRP and GFRP. They can be robust, when used appropriately and have shown to deliver more information than some traditional gauges (more than strain value). As the use of FRP for critical infrastructure increases, so will these innovative ways to monitor them.

References

AS 5100, Australian Standards, Bridge Design Code, 2012.

Bunsell, A and Renard, J, 2005, *Fundamentals of fibre reinforced composite materials*, IOP Publishing Ltd, UK

Campbell, FC, 2010, Structural Composite Materials: Chapter 1: Introduction to Composite Materials, ASM International.

Cusano, A, Cutolo, A, Albert, J, 2011, Fiber Bragg Grating Sensors: Recent Advancements, Industrial Applications and Market Exploitation, Bentham Science Publishers.

Epaarachchi, J, Canning, J, Stevenson, M, 2009, The response of embedded NIR (830nm) fiber bragg grating sensors in glass fiber composites under fatigue loading, Journal of composite materials, September 2009.

Fitzpatrick, T, 2001, *Linking London: The Millennium Bridge*, Royal Academy of Engineering.

Hill, PC and Eggleton, BJ 1994, *Strain gradient chirp of fiber Bragg gratings*, Electronics Letters, vol.30, no.14, pp. 1172–1174.

Hollaway, L.C. 2003, The evolution of and the way forward for advanced polymer composites in the civil infrastructure, Composites and Building Materials, vol. 17, pp. 365-378.

Kahandawa, G.C, Epaarachchi, J, Wang, H and Canning, J, 2010, Effects of the self-distortions of embedded FBG sensors on spectral response due to torsional and combined loads, APWSHM 3, November 2010

Kahandawa, G.C., Epaarachchi, J, Wang, H, Lau,K.T., 2012, *Use of FBG Sensors for SHM in Aerospace Structures*, Photonic Sensors 2012,vol 2, no.3.

Kashyap, R 1999, Fibre Bregg gratings, Academic Press Publications.

Keulen, CJ, Yildiz, M, Suleman, A, 2011. Multiplexed FBG and etched fiber sensors for process and health monitoring of 2-&3-D RTM components

Kim, SD, Kwon, OJ and Han, YG, 2012, Long distance fiber Bragg grating strain sensor interrogation using high speed Raman-based Fourier domain mode-locked fiber laser with recycled residual Raman pump, Caltec.

Marshall, DB and Cox, BN 1985, *The mechanics of matrix cracking in brittle-matrix fiber composites*, Acta Metallurgica, vol.33, no.11, pp.2013-2021.

Mizutani, Y, Groves, RM, 2011, *Multi-Functional Measurement Using a Single FBG Sensor*, Experimental Mechanics.

Nakamura, T, Igawa, H, Kanda, A, 2011, Inverse Identification of continuously distributed loads using strain data, Aerospace Science and Technology 23, 2011.

Nelson, B.A, 2014, *Composites: State-of-Art in Pedestrian Bridges*, 6th Australian Small Bridges Conference 2014, Comstrat Australasia.

Netcomposites, 2014, Infusion Processes, Date Viewed: 12th November 2014, URL: <http://www.netcomposites.com/guide/infusion-processes/57>

Rodrigues, C, Félix, C, Lage, A, Figueiras, J, 2010, Development of a long-term monitoring system based on FBG sensors applied to concrete bridges, Engineering Structures, Elsevier.

Sarazin, GA, Newhook, JP, 2006, *A strain-based index for monitoring laminates of FRP-strengthened beams*, Construction and Building Materials 21, Eslevier.

Takeda, S, Okabe, Y, Takeda, N, 2008, *Monitoring Delamination Growth in CFRP laminates using chirped FBG sensors*, Journal of Intelligent material systems and structures.

Tomishenko, S, 1972, *Mechanics of Materials* , with J. M. Gere, 1st edition, D. Van Nostrand Company.

Appendix A: List of Figures

Appendix B: List of Tables

Appendix C: Production Drawing

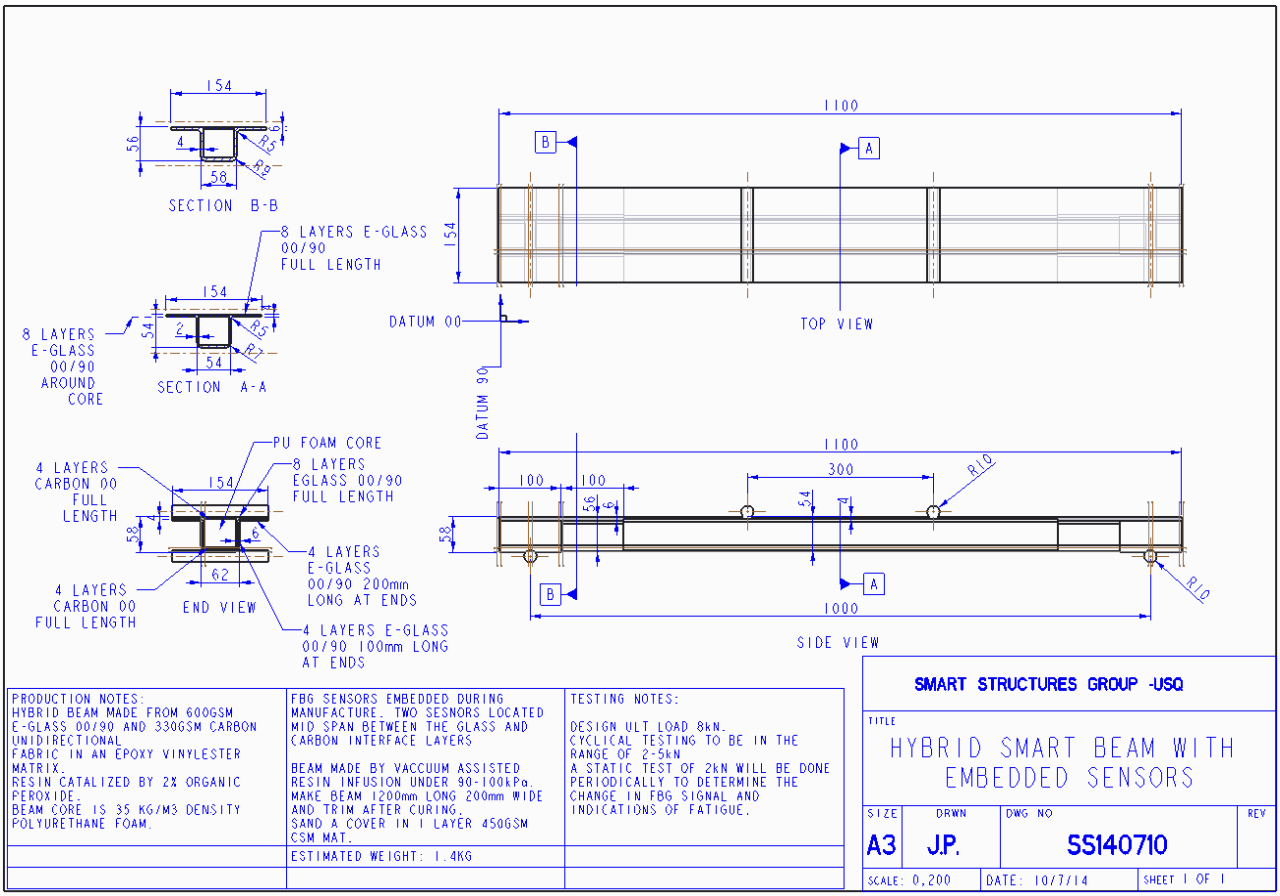

Appendix D: FEA Plots

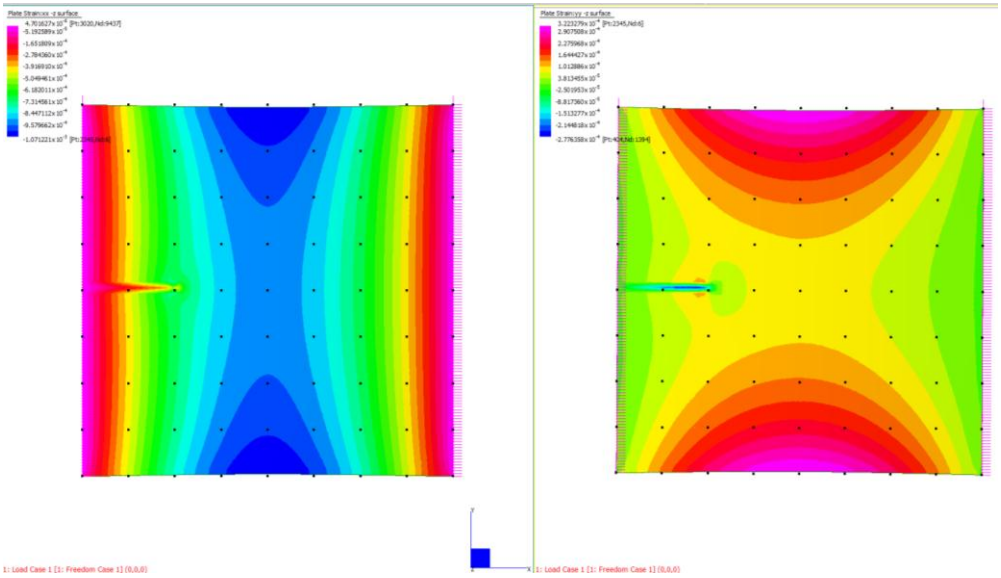

Figure 6-1: Strain Plot of SS Deck on 2 sides under UDL with Damage at support edge

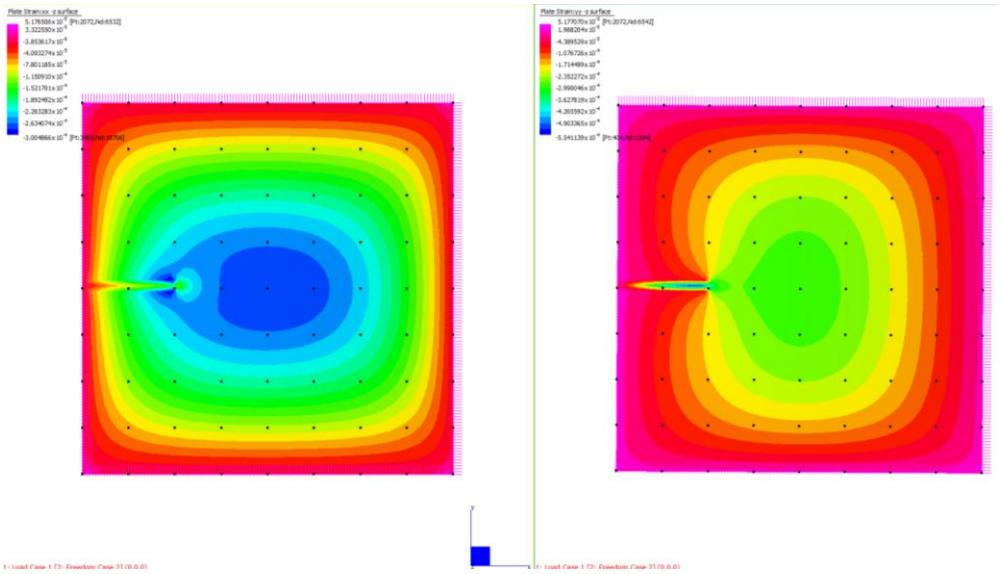

Figure 6-2: Strain Plot of SS Deck on 4 sides under UDL with Damage at support edge

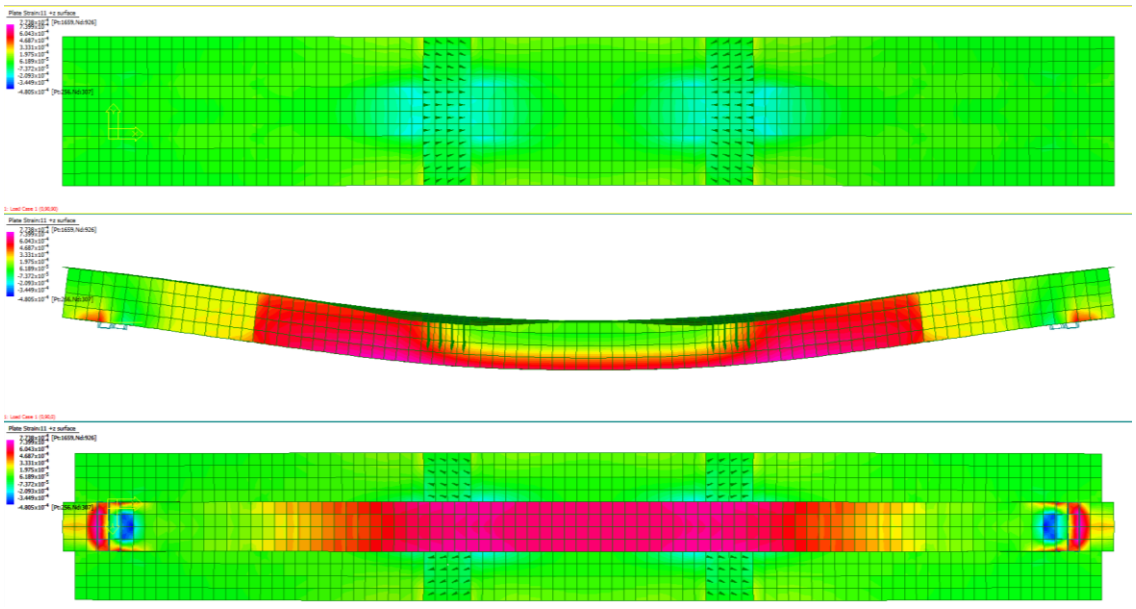

Figure 6-3: Strain Distribution in longitudinal direction xx

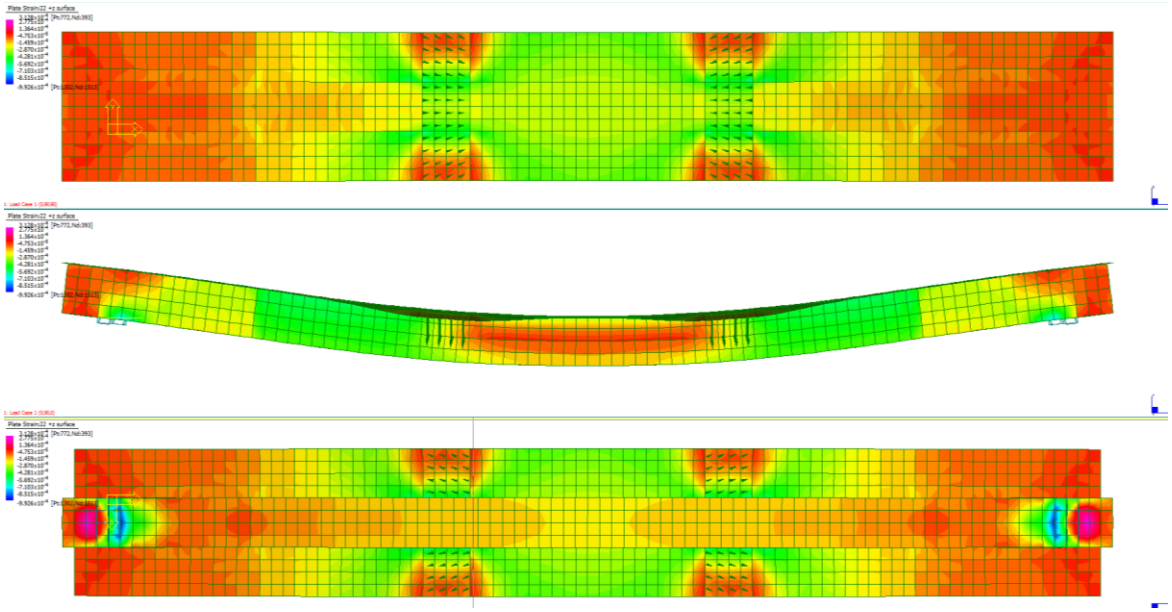

Figure 6-4: Strain distribution in vertical direction yy

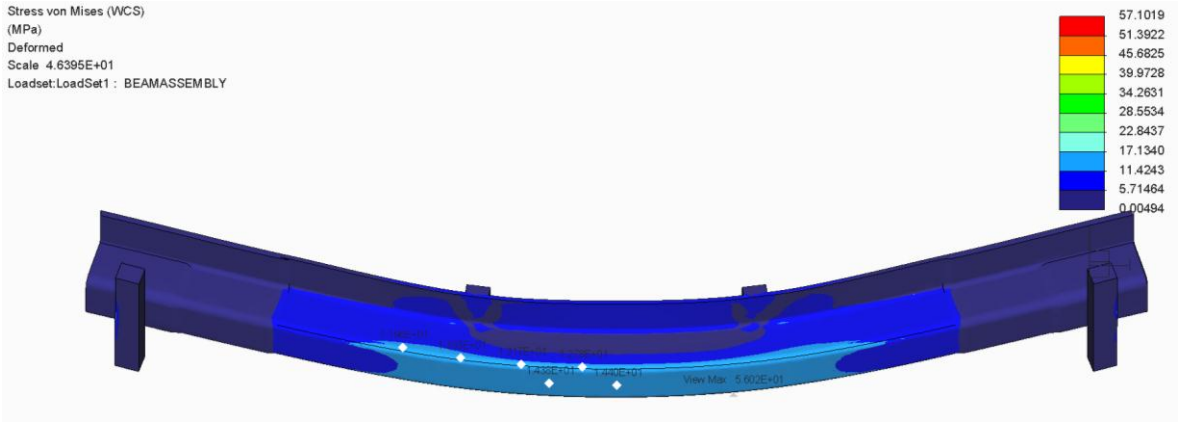

Figure 6-5: Stress Distribution for FPB in Creo

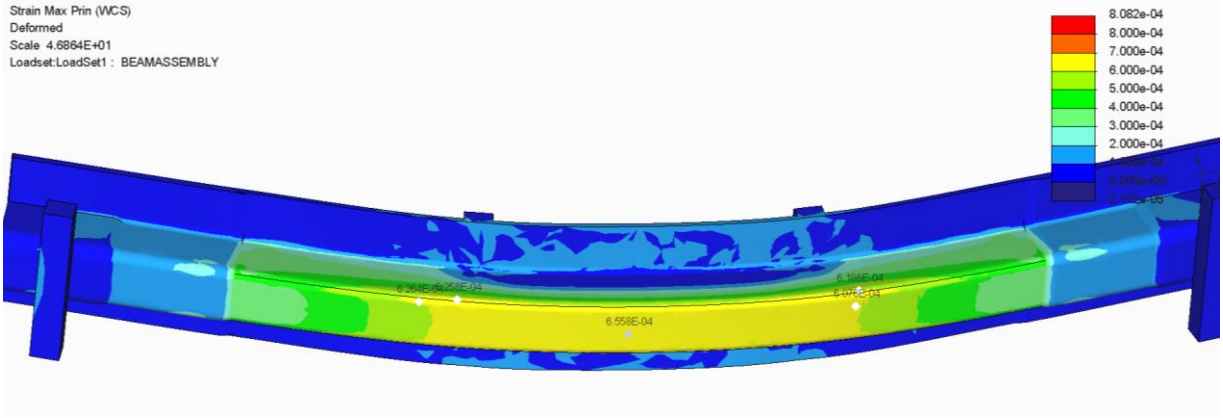

Figure 6-6: Strain Distribution for FPB in Creo